Investigation of Physiological Pulsatile Flow in a Model Arterial Stenosis Using Large-Eddy and Direct Numerical Simulations

M. C. Paul *and M. M. Molla
CFD Group, School of Engineering, University of Glasgow,
Glasgow G12 8QQ, UK

Abstract

Physiological pulsatile flow in a 3D model of arterial stenosis is investigated by using Large Eddy Simulation (LES) technique. The computational domain chosen is a simple channel with a biological type stenosis formed eccentrically on the top wall. The physiological pulsation is generated at the inlet using the first harmonic of the Fourier series of pressure pulse. In LES, the large scale flows are resolved fully while the unresolved subgrid scale (SGS) motions are modelled using a localized dynamic model. Due to the narrowing of artery the pulsatile flow becomes transition-to-turbulent in the downstream region of the stenosis, where a high level of turbulent fluctuations is achieved, and some detailed information about the nature of these fluctuations are revealed through the investigation of the turbulent energy spectra. Transition-to-turbulent of the pulsatile flow in the post stenosis is examined through the various numerical results such as velocity, streamlines, velocity vectors, vortices, wall pressure and shear stresses, turbulent kinetic energy, and pressure gradient. A comparison of the LES results with the coarse DNS are given for the Reynolds number of 2000 in terms of the mean pressure, wall shear stress as well as the turbulent characteristics. The results show that the shear stress at the upper wall is low just prior to the centre of the stenosis, while it is maximum in the throat of the stenosis. But, at the immediate post stenotic region, the wall shear stress takes the oscillating form which is quite harmful to the blood cells and vessels. In addition, the pressure drops at the throat of the stenosis where the re-circulated flow region is created due to the adverse pressure gradient. The maximum turbulent kinetic energy is located at the post stenosis with the presence of the inertial sub-range region of slope $-5/3$.

Keywords: Physiological pulsatile flow, Arterial stenosis, Transition-to-turbulent flow, LES, DNS

*E-mail: Manosh.Paul@glasgow.ac.uk, Tel:+44 (0)141 330 8466, Fax:+44 (0)141 330 4343

1 Introduction

In the presence of a stenosis in an artery the flow nature in the downstream region of stenosis is significantly changed, and the separated flow from the stenosis strongly depends on the degree of the stenosis and the physiological pulsatile flow conditions. Due to the presence of a moderate or severe stenosis and the pulsatile flow, highly disturbed flow occurs in the downstream of stenosis, and consequently, the flow pattern becomes very irregular and complex as it transits to turbulent. To get a better insight on the transition-to-turbulent flow through the arterial stenosis, the research in this area is increased in the recent years due to the rapid evolution of the sate-of-the-art computing facilities. Our study focuses on the transition of physiological pulsatile flow through a model of arterial stenosis by using Direct Numerical Simulation (DNS) and Large-Eddy Simulation (LES) techniques.

Ku [1] described in his review article that the blood flow exhibits non-Newtonian behaviour in small branches of artery and capillaries where the blood cells squeeze through and a cell-free skimming layer reduces the effective viscosity through the artery. However, the blood in most arteries behaves as a Newtonian fluid where the viscosity can be taken as a constant. The typical Reynolds number for the blood flow varies from 1 in small arteries to approximately 4000 in large arteries, and due to the cyclic nature of the heart pump the blood flow is always unsteady and much challenging to investigate properly.

Lees and Dewey [2] studied the fluid motion in arteries narrowed by atherosclerosis by using a non-invasive diagnostic method "Phonoangiography". They concluded that the arterial sounds produced by turbulence create distal to the localized arterial stenosis. Clark [3, 4] performed the experimental studies of the pulsatile flow in a model of aortic stenosis taking the Reynolds number between 740 and 1500. He showed the existence of an inertia subrange region by the spectral analysis of turbulent fluctuations found in the post stenosis region. On the other hand, imposing the steady flow Tobin and Chang [5] investigated the wall pressure spectra at the post stenotic region for understanding the arterial murmur sounds due to the flow disturbances. They reported that the frequency of the post stenotic pressure spectra lies between 20 and 1000 Hz and the corresponding Strouhal number lies from 0.1 to 2. This, relative high, frequency is responsible for the arterial murmur sounds.

Khalifa and Giddens [6, 7] investigated the post stenotic disturbances by using laser doppler anemometer (LDA) technique. In their experiments, they used a sinusoidal velocity oscillation in the inlet of the model and their analysis on the disturbance energy spectra showed the similar types of result reported by Clark [3]. In the further studies, Ahmed and Giddens [8, 9, 10] and Ahmed [11] investigated the post stenotic flow behaviour with both steady and pulsatile natures of the flow by using the LDA approach and they measured the velocity and velocity disturbances at the post stenosis region.

Computational studies have been done by several authors: Brien and Ehrila [12] studied the simple pulsatile flow through an arterial stenosis; Tutty [13] investigated the pulsatile flow in a circular constricted channel and showed the variation of the wall pressure, wall shear stress and flow pattern at the different phases of the flow pulsation; Tu *et al.* [14] and Deplaon and Siouffi [15] studied the flow characteristics

using the simple pulsatile flow through a stenosis. A study of the steady laminar flow through tubes with multiple stenoses has been done by Damodaran *et al.* [16]. The physiological and simple pulsatile flows through an axisymmetric arterial stenosis have been investigated by Zendehbudi and Moayeri [17]. The above mentioned computational studies are related to the 2D laminar flow.

Dvinsky and Ojha [18] simulated the 3D pulsatile flow through an asymmetric stenosis. They used a sinusoidal pulsation flow and showed only the post stenotic velocity pattern. Rheological effects on the transient laminar axisymmetric pulsatile flow through a tube with stenosis have been studied by Buchanan *et al.* [19]. Long *et al.* [20] investigated the physiological pulsatile laminar flow through the arterial stenosis with relatively low Reynolds number and found that the wall shear stress oscillates between negative and positive values at the post stenotic region. Neofytou and Tsangaris [21] showed the rheological effects on the steady flow through the arterial stenosis and aneurysm. Laminar to turbulent transition and the instability of the pulsatile flow have been studied by Mallinger and Drikakis [22, 23] by considering the maximum Reynolds number of 1245. They also found that the wall shear stress at the post stenotic region oscillates between the negative and positive values, but in their studies they did not provide any information about the turbulent random fluctuations which are quite important issues in the pathological point of view.

Ghalichi *et al.* [24] and Lee *et al.* [25, 26] carried out some axisymmetric computational studies of 2D laminar to turbulent flow by using the Reynolds-average Navier-Stokes (RANS) approach, particularly, the k-ω turbulence model. But Scotti and Piomelli [27] clearly indicated the limitations of using the conventional RANS turbulent models to study pulsatile flows. These models are not capable of predicting the time accurate flow as the governing equations of motion are time-averaged. The LES approach, which lies somewhat between DNS and RANS, has already proved to be an excellent technique for modelling turbulent flow. In DNS, all the large and small scales are resolved, but in LES, only the large scales, i.e. the energy-containing scales of turbulence are resolved while the smaller or sub-grid scales (SGS) are modelled. DNS is suitable for a low Reynolds number flow but LES is applicable for a small to high Reynolds number flow and requires less time and mesh than DNS, since in LES the smallest scales need not to be resolved. The application of LES in the modelling of transient physiological flow through stenosis is very limited. The most recent studies of Paul *et al.* [28, 29] and Mittal *et al.* [30] show that the LES could be an ideal simulation technique for studying the transition of the pulsatile flow.

The aim of this paper is to perform both Large-Eddy and Direct Numerical Simulations to investigate the post-stenotic transition-to-turbulent behaviours of the physiological pulsatile flow through a stenosis. The eccentric stenosis which is formed on the top wall of the channel is simple but biologically realistic. Though the flow physics are understood to some extent from the previous studies, it is hoped that both the LES and DNS would provide some in-depth and additional information about the turbulent flow downstream of the stenosis. The Piomelli-Liu localized dynamic model, [31], is applied in the LES for modelling the SGS motions. Some important turbulent results such as oscillatory wall shear stress, root mean square turbulent fluctuations as well as turbulent kinetic energy are presented in

the paper, which facilitate to understand the nature and level of the turbulent flow present in the post-stenosis.

2 Formation of the problem

2.1 Model geometry

The geometry shown in Fig. 1 consists of a 3D channel with one-sided cosine shape stenosis on the upper wall centred at $y/L = 0.0$, where y is the horizontal distance or the distance along the flow and L is the height of the channel. In the model the height (x) and its width (z) are kept same and the length of the stenosis is equal to twice of the channel height. The length of the channel is $5L$ before the stenosis, while $15L$ is the downstream region of the stenosis. The formation of the stenosis chosen for this study as

$$\frac{x}{L} = 1 - \frac{\delta_c}{2}\left(1 + \cos\frac{y\pi}{L}\right), \quad -L \leq y \leq L \tag{1}$$

where δ_c is the parameter for controlling the percentage of the stenosis. In the present paper, δ_c is fixed to $\frac{1}{2}$, which gives a 50% reduction of the cross-sectional area at the centre of the stenosis. The smooth constriction/stenosis generated at the channel using relation (1) gives a fairly reasonable representation of an arterial stenosis (or biological stenosis), see [32].

2.2 Governing equations

It is quite acceptable that the blood flow in a large vessel may be modelled accurately as a Newtonian fluid according to Pedley [33], which refers to the use of the Navier-Stokes equations of motion for investigating the post stenotic flow-physics of blood through the arterial stenosis. We also assume that the fluid is homogeneous and incompressible. In DNS the Navier-Stokes equations are solved directly using the numerical techniques presented in Section 3, whereas in LES the equations of motion are obtained by applying a spatial filter, namely the *grid*-filter, a mechanism to separate the large-scale variables, i.e. the resolved quantities, from the small scales. After applying the filter function to the Navier-Stokes equations of motion, we obtain the following filtered equations [31]:

$$\frac{\partial \bar{u_j}}{\partial x_j} = 0, \tag{2}$$

$$\frac{\partial \bar{u_i}}{\partial t} + \frac{\partial \bar{u_i}\bar{u_j}}{\partial x_j} = -\frac{1}{\rho}\frac{\partial \bar{p}}{\partial x_i} + \frac{\partial}{\partial x_j}\left[\nu\left(\frac{\partial \bar{u_i}}{\partial x_j} + \frac{\partial \bar{u_j}}{\partial x_i}\right)\right] - \frac{\partial \tau_{ij}}{\partial x_j}, \tag{3}$$

where $\bar{u_i}$ is the velocity vector along $x_i = (x, y, z)$, $\bar{p}$ is pressure, t is time, $\rho = 1.05 \times 10^3$ kg·m^{-3} is density, and ν is the kinematic viscosity obtained from the viscosity $\mu = 3.45 \times 10^{-3}$ Pa.s and ρ. The effects of the small scale appear in the subgrid-scale stress (SGS) term as

$$\tau_{ij} = \overline{u_i u_j} - \bar{u_i}\bar{u_j}, \tag{4}$$

which is modelled as (Smagorinsky [34]),

$$\tau_{ij} - \frac{1}{3}\delta_{ij}\tau_{kk} = -2(C_s\triangle)^2|\bar{S}|\bar{S_{ij}}, \tag{5}$$

where $\triangle = \sqrt[3]{\triangle x \triangle y \triangle z}$ is the filter width and $|\bar{S}| = \sqrt{2\bar{S_{ij}}\bar{S_{ij}}}$ is the magnitude of the large scale strain rate tensors defined as $\bar{S_{ij}} = \frac{1}{2}\left(\frac{\partial \bar{u_i}}{\partial x_j} + \frac{\partial \bar{u_j}}{\partial x_i}\right)$. The unknown Smagorinsky constant, C_s, is calculated using the localized dynamic model of Piomelli and Liu [31].

2.3 Boundary conditions and mesh distribution

The physiological pulsatile laminar velocity profile, which is used to generate the time-dependent pulsatile flow at the inlet of the channel, is obtained via the analytic solution of the one-dimensional form of the Navier-Stokes equation in the streamwise direction taking the pressure gradient as a Fourier series in time (Womersley [35] and Loudon and Tordesillas [36]). Some brief details on the derivation of the physiological pulse are given below.

The Navier-Stokes equation in the streamwise direction can easily be written as

$$\frac{\partial^2 \bar{v}}{\partial x^2} - \frac{\rho}{\mu}\frac{\partial \bar{v}}{\partial t} = \frac{1}{\mu}\frac{\partial \bar{p}}{\partial y}, \quad 0 \le x \le L \tag{6}$$

where the pressure gradient for the physiological pulsation is defined as

$$\frac{\partial \bar{p}}{\partial y} = \frac{2}{3}A_0 + A\sum_{n=1}^{N} M_n e^{i(n\omega t + \phi_n)}. \tag{7}$$

The constants, A_0 and A, appeared in (7) correspond to the steady and the oscillatory parts of the pressure gradient, respectively. M_n and ϕ_n are the respective coefficients and the phase angle where N gives the number of harmonics of the physiological flow; and ω is the frequency of the unsteady flow.

The solution of Eq. (6) takes the following form:

$$\bar{v}(x,t) = 4\bar{V}\frac{x}{L}\left(1 - \frac{x}{L}\right) + A\sum_{n=1}^{N}\frac{iM_nL^2}{\mu\alpha^2 n} \left[\cosh(\alpha\sqrt{in}\frac{x}{L}) - \frac{\cosh(\alpha\sqrt{in}) - 1}{\sinh(\alpha\sqrt{in})}\sinh(\alpha\sqrt{in}\frac{x}{L}) - 1\right] e^{i(n\omega t + \phi_n)}. \tag{8}$$

The real part of this solution (8) is used as an inlet boundary condition to generate the physiological flow through the channel. In the solution, the bulk velocity, $\bar{V}$, depends on the flow Reynolds number which is defined as $Re = \frac{\bar{V}L}{\nu}$; and $\alpha = L\sqrt{\frac{\rho\omega}{\mu}}$ is the unsteady Reynolds number or the Womersley number which gives the ratio of the unsteady forces to the viscous forces. Note that when the Womersley number is relatively small, the viscous forces usually dominate flow. The unsteady inertia forces take an important role in the physiological flow when $\alpha > 10$, see Ku [1]. In our simulation we have used $\alpha = 10.5$ and $N = 1$ (first harmonic of the pressure pulse).

The value of the amplitude of oscillation, A, is varied with the Reynolds number to maintain the maximum flow rate at the inlet. For Re = 1000, 1400, 1700 and 2000; the values of A are taken as 0.25, 0.3, 0.35 and 0.4 respectively. In addition, the pulsatile coefficient, M_n, takes a value of 0.78 and the phase angle, ϕ_n, is equal to 0.0113446 when $N = 1$. These values are taken from the paper of Womersley [35].

The inlet pulsatile velocity profile derived from the above relation (8) is presented in Fig. 2 for the Reynolds number of 2000. In frame (a) the velocity at a full pulsation is shown which is recorded at the centre of the inlet plane, while the variation of this between the top and bottom planes at different phase during the pulsation is shown in frame (b). It is interesting to observe that the oscillating part of the pressure pulse has created the negative velocity (back flow) close to the channel walls during the diastolic phase (e.g. at $t/T = 0.5$, 0.625 and 0.75).

No slip boundary conditions are used for both the lower and upper walls of the model, and at the outlet a convective boundary condition is used as

$$\frac{\partial \bar{u}_i}{\partial t} + U_c \frac{\partial \bar{u}_i}{\partial y} = 0, \tag{9}$$

where U_c is the convective velocity which takes the constant mean exit velocity. For the spanwise boundaries, periodic boundary conditions are applied for modelling the spanwise homogeneous flow. Non-uniform dense meshes are used near both the top and bottom walls of the model to accurately capture the thin shear layer that is developed in the vicinity of the walls (Fig. 3). In addition, the meshes are concentrated at the region immediate downstream of the stenosis where the flow separation takes place.

3 Numerical procedures

The governing filtered equations (2-3) in the Cartesian coordinates are transformed into the curvilinear coordinate system and the finite volume approaches are used to discretised the partial differential equations to yield a system of quasi-linear algebraic equations. To discretise the spatial derivatives in Eqs. (2-3), the standard second order accurate central difference scheme is used, except for the convective terms in the momentum equations (3) for which an energy conserving discretisation scheme is used [37].

Time derivatives are discretised by a three point backward difference scheme with a constant timestep of δt, which is represented by

$$\frac{\partial \mathbf{u}}{\partial t} \approx \frac{3}{2}\left(\frac{\mathbf{u}^{n+1} - \mathbf{u}^{n}}{\delta t}\right) - \frac{1}{2}\left(\frac{\mathbf{u}^{n} - \mathbf{u}^{n-1}}{\delta t}\right). \tag{10}$$

The pressure and velocity fields are obtained by employing a pressure correction method which is similar to the SIMPLE algorithm of Patankar [38]. This method is briefly explained below.

The finite difference equation of the u-momentum equation to within the second order accuracy can be written in the following quasi-matrix form

$$\mathbf{u}^{n+1} - \mathbf{u}^{n} + \frac{2}{3}\delta t \mathbf{T}^{n+1}\mathbf{u}^{n+1} = -\frac{2}{3}\delta t \mathbf{D}\mathbf{p}^{n+1} + \mathbf{S}, \tag{11}$$

where $\mathbf{u}$ is the vector of the unknown u nodal values, $\mathbf{T}^{n+1}$ is the finite difference coefficient of the convection and diffusion terms at $n+1$, $\mathbf{D}$ corresponds to the discretisation of the pressure term, and the source term $\mathbf{S}$ contains all the remaining terms including the cross-stresses not contained within $\mathbf{T}^{n+1}$ which have been treated explicitly to reduce the computational cost.

In order to maintain a second order accuracy, Eq. (11) is solved in two stages. In the first stage, a pressure increment as $\Delta\mathbf{p}^m = \mathbf{p}^m - \mathbf{p}^n$ is introduced so Eq. (11) becomes

$$(\mathbf{I} + \frac{2}{3}\delta t\mathbf{T}^n)\underbrace{(\mathbf{u}^m + \frac{2}{3}\delta t\mathbf{D}\Delta\mathbf{p}^m)}_{\mathbf{u}^*} = -\frac{2}{3}\delta t\mathbf{D}\mathbf{p}^n + \mathbf{S}, \tag{12}$$

where m represents an intermediate time level between $n+1$, at which the solution is sought, and n, the most recent update. Then the system of equation (12) is solved in the following two steps:

$$\mathbf{u}^* = (\mathbf{I} + \frac{2}{3}\delta t\mathbf{T}^n)^{-1}(-\frac{2}{3}\delta t\mathbf{D}\mathbf{p}^n + \mathbf{S}), \tag{13}$$

$$\mathbf{u}^m = \mathbf{u}^* - \frac{2}{3}\delta t\mathbf{D}\Delta\mathbf{p}^m. \tag{14}$$

The vectors of unknown v and w nodal values, $\mathbf{v}$ and $\mathbf{w}$, are obtained in the similar way. However, none of these velocity fields at time level m can be obtained since $\Delta\mathbf{p}^m$ is not known. In order to obtain the pressure increment $\Delta\mathbf{p}^m$, the velocity fields $\mathbf{u}^m$, $\mathbf{v}^m$ and $\mathbf{w}^m$ are substituted into the continuity equation, giving a Poission-type equation for the pressure increment. Since $\mathbf{u}^m$ is a second order accurate approximation to $\mathbf{u}^{n+1}$, in the second stage, a second order accurate solution at the time level $n+1$ is obtained by rewriting the equation (12) for the time level $n+1$, with the coefficient matrix is evaluated using the most recent update for the flow field obtained at time level m,

$$(\mathbf{I} + \frac{2}{3}\delta t\mathbf{T}^m)\underbrace{(\mathbf{u}^{n+1} + \frac{2}{3}\delta t\mathbf{D}\Delta\mathbf{p}^{n+1})}_{\mathbf{u}^{**}} = -\frac{2}{3}\delta t\mathbf{D}\mathbf{p}^m + \mathbf{S}. \tag{15}$$

Again, Eq. (15) is solved in two steps:

$$\mathbf{u}^{**} = (\mathbf{I} + \frac{2}{3}\delta t\mathbf{T}^m)^{-1}(-\frac{2}{3}\delta t\mathbf{D}\mathbf{p}^m + \mathbf{S}) \tag{16}$$

$$\mathbf{u}^{n+1} = \mathbf{u}^{**} - \frac{2}{3}\delta t\mathbf{D}\Delta\mathbf{p}^{n+1}. \tag{17}$$

Using the above mentioned pressure correction algorithm, the computed pressure and the velocity components are stored at the centre of a control volume according to the collocated grid arrangement. The Poisson like pressure correction equation is discretised by using the Rhie and Chow [39] pressure smoothing approach, which prevents the even-odd node uncoupling in the pressure and velocity fields. The BI-CGSTAB [40] solver is used for solving the matrix of velocity vectors, while for the Poisson like pressure correction equation an ICCG [41] solver is applied due to its symmetric and positive definite nature. The code is second order accurate in both time and space and has been applied extensively in other engineering flows [42, 43, 44, 45], more details about the numerical algorithm can be found in those published papers and also in Molla [46].

4 Data processing

In the data processing, some different types of averaging procedure have been used. For a generic flow filtered variable, $\bar{f}$, the mean over the total number of timestep N_t is calculate as

$$< f > (x, y, z) = \frac{1}{N_t} \sum_{i=1}^{N_t} \bar{f}(x, y, z, t_i). \tag{18}$$

In order to separate the turbulent fluctuations from the pulsatile fluctuations, a phase averaging technique is applied (Hussain and Reynolds [47] and Lieber and Giddens [48]). The phase average over $T_f = NT$, where N is the total number of periods and T is the time period, is computed as

$$<< f >> (x, y, t) = \frac{1}{N} \sum_{n=0}^{N-1} < f >_s (x, y, t + nT), \tag{19}$$

where $< f >_s$ is the spanwise average quantity of $\bar{f}$ defined as

$$< f >_s (x, y, t) = \frac{1}{L_3} \int_0^{L_3} \bar{f}(x, y, z, t) dz, \tag{20}$$

where L_3 is the total number of mesh points used in the spanwise direction. Finally, the random turbulent fluctuations are computed using

$$f''(x, y, z, t) = \bar{f}(x, y, z, t) - << f >> (x, y, t). \tag{21}$$

Thus, the root mean square (rms) values of the turbulent fluctuations are calculated using the following definition

$$< f'' >_{rms} = \sqrt{< f''^2 >}. \tag{22}$$

5 Results and discussion

In the present study the Reynolds numbers ranging from 1000 to 2000 are considered and the area reduction of the channel due to the stenosis is fixed at 50%. Various simulations with the LES and DNS have been performed using the various grid arrangements and timesteps, Table 1 shows a list of the simulation details. The results of the grid and timestep independence tests are presented in § 5.1. The roles of the dynamic sub-grid model, such as the contributions of the model constant C_s and the SGS eddy viscosity, are presented in § 5.2. In § 5.3 and § 5.4, the results of the instant and mean flow physics are presented, respectively. In-depth investigations of the turbulent flow downstream on the stenosis are performed and the results are summarised in § 5.5.

5.1 Grid and timestep independence tests

The grid and timestep independence tests have been carried out to establish a suitable combination of the grid configuration and timestep that is required for the

Table 1: Grid details for the LES and DNS approaches.

Case	Re	Approach	N_x	N_y	N_z	δt
0	< 2000	LES	50	200	50	1.0×10^{-3}
1	2000	LES	50	200	50	1.0×10^{-3}
2	2000	LES	50	250	50	1.0×10^{-3}
3	2000	LES	50	300	50	1.0×10^{-3}
4	2000	LES	70	250	50	1.0×10^{-3}
5	2000	DNS	50	350	50	1.0×10^{-3}
6	2000	DNS	70	350	50	1.0×10^{-3}
7	2000	LES	50	200	50	1.5×10^{-3}
8	2000	LES	50	200	50	2.0×10^{-3}

LES to adequately resolve the physiological flow in the stenosis. Initially, fixing the Reynolds number (Re) at 2000 and the timestep (δt) at 10^{-3}, four computations have been performed with the LES by using the four different grid setups: $50 \times 200 \times 50$ (Case 1), $50 \times 250 \times 50$ (Case 2), $50 \times 300 \times 50$ (Case 3) and $70 \times 250 \times 50$ (Case 4), respectively, see Table 1. The results of these four cases are compared in Figs. 4 and 5 in terms of the mean streamwise velocity, $< \bar{v} > /\bar{V}$, and the turbulent kinetic energy (TKE), $\frac{1}{2} < u_j'' u_j'' > /\bar{V}^2$, respectively, at the different axial positions along the flow. Note that, for Cases 1-6, when the number of grid points along the streamwise direction (N_y) is increased, particular attention is paid onto the accurate capturing of the small scale turbulent eddies at the post-stenosis regime. For that, the number of streamwise grid points before the stenosis is always kept fixed at 50 while the rest of the total grid points of N_y is distributed in the post stenosis region.

As can be seen in Fig. 4, the grid configurations used in the LES (Cases 1-4) are sufficient to resolve the mean streamwise velocity, and their comparisons with the two coarse DNS results (Cases 5,6) also show excellent agreement. However, Fig. 5 shows that the results of the turbulent kinetic energy at the immediate post stenotic region, $1 < y/L < 6$ (frames c-j), are slightly sensitive to the choice of grids in LES since only the resolved scale flows are computed in LES by the grid resolution. Thus, a totally grid independence of the computed turbulent random fluctuations is not expected in LES and it is adequate to prove in LES that the primary flow features (mean velocities) do not vary significantly with the grid. The dependence remains apparent until the grid resolution becomes fine enough that the LES starts to qualify as DNS.

The timestep δt in Case 1 is now varied from 10^{-3} to 1.5×10^{-3} (Case 7) and 2.0×10^{-3} (Case 8), and the results are compared in Fig. 6 in terms of the centreline mean kinetic energy $\frac{1}{2} < \bar{u}_j \bar{u}_j > /\bar{V}^2$ (frame a) and the turbulent kinetic energy (frame b). From this figure it is seen that the results before the stenosis are quite independent to the timesteps used, however, at the post stenotic region, where the flow is turbulent, the results are slightly sensitive. In the simulation of a turbulent flow the timestep usually depends on the grid size, therefore, fixing one grid resolution it is reasonable to get some sensitivities in the turbulent results for the different timesteps (Choi and Moin [49]). To avoid any unstable solutions for

the different types of grid resolution, the smallest timestep of 10^{-3}, was chosen in the computation, by ensuring that the maximum Courant number lies between 0.1 and 0.2. Also based on the satisfactory grid independence test in Figs. 4 and 5 for $Re = 2000$, the simulations for the other Reynolds numbers less than 2000 have been performed with $50 \times 200 \times 50$ (Case 1).

5.2 Contribution of the SGS model

Fig. 7(a-d) represent the contour plots of the sub-grid scale (SGS) model parameter C_s in the $x - y$ middle plane for the different Reynolds numbers. The results show that the maximum value of the dynamic Smagorinsky constant, C_s, clearly depends on the flow Reynolds number and increases as the Reynolds number is increased. For example, when $Re = 1000$ (frame a) the maximum value of C_s is found approximately 0.053, while for the other Reynolds numbers, $Re = 1400$, 1700 and 2000, the respective maximum value of C_s is about 0.071, 0.098 and 0.106 which are very close to the typical value of the model constant 0.1 used by many previous LES investigations of channel flow. Moreover, it is also important to find that the maximum value of C_s occurs at the post stenotic region where the nature of the flow is predicted to be turbulent. The values of C_s before the stenosis are very small due to the laminar nature of the flow, therefore, it is quite clear from these results that the dynamic procedure is well coped of calibrating the SGS stresses properly in the model.

The corresponding eddy viscosity, μ_{sgs}, normalized by the molecular viscosity, μ, is depicted by Fig. 8. In frame (a), the maximum eddy viscosity of about 0.069 indicates that the maximum contribution of the SGS model in the LES is approximately 6.9%. The contribution of the SGS model increases with the Reynolds number which is shown in frames (b-d). For $Re = 1400$, 1700 and 2000, a maximum eddy viscosity of about 0.182, 0.292 and 0.374 is received from the SGS model respectively, in other words, the large scale motion receives a maximum of 18.2%, 29.2% and 37.4% contribution from the SGS model. Moreover, from the colour bar it is also seen that the maximum SGS dissipation occurs at the post stenotic region.

5.3 Instantaneous flow field

In Fig. 9 the cycle-to-cycle flow development is shown by the contour plots of the streamwise velocity, $\bar{v}$, for $Re = 2000$. In frame (a) it is observed that at the end of the first cycle a small re-circulation region or a primary shear layer which is initially created between the centre and the post-lip of the stenosis elongates towards the downstream after the end of the second cycle, frame (b), where the creation of a secondary shear layer is observed near the lower wall. As the flow progresses with time, these two shear layers interact with each other and finally break down into vortices which then move towards the downstream, shown clearly in frames (c-g). As a result, the nature of the transient/separated flow downstream of the stenosis is observed turbulent. We note here that the simulation has been carried out up to the end of the eleventh cycle, as it has been tested that the solutions eventually reach to a stationary state after the eighth cycle, and the mean results, which are

accumulated after the fourth cycle and presented in the next section, do not vary significantly between the eighth and eleventh cycles. Also the instant turbulent flow pattern at the downstream of stenosis doesn't show any rigorous change at the end of cycles after eight.

While in Fig. 9 the development of the instant flow at the end of various cycles is presented in the mid-horizontal plane, Fig. 10 shows the cross-sectional view of the flow streamlines of Fig. 9(h) in the different streamwise locations. The streamlines at the inlet of the channel clearly indicate that the flow pattern is laminar (frame a) since there is no intersection between the streamlines. Frame (b), on the other hand, shows that the flow at the centre of the stenosis is still laminar but about to transit close to the lower wall. At the post-lip of the stenosis, at $y/L = 1$ (frame c), the transitional behaviour of the flow near the upper wall is evident, and the flow patterns in the subsequent frames plotted at $y/L = 2$ to 10 are very chaotic. Note that Frydrychowicz *et al*. [50] in their investigation of the aortic vascular hemodynamics with stenosis using the 4D MRI technique termed the formation of these complex vortices or flow features as "corkscrew". The intensity of the turbulent nature of this flow will be examined later in § 5.5.

The effects of the Reynolds number on the development of the flow along the streamwise direction are presented in Fig. 11 at $t/T = 10.25$, which is the position of the peak pulse. In this figure, the streamwise velocity vectors are appended on the contours of the streamwise velocity $\bar{v}/\bar{V}$, at $z = L/2$. We find that, for all the Reynolds numbers, the large primary re-circulation region develops near the post-lip of the stenosis due to the separation of the shear layer from the nose of the stenosis. The region of this re-circulation extends to the streamwise direction as the Reynolds number is increased. Moreover, the primary re-circulation zone after the stenosis is found permanent and has some important medical consequences, as it increases the staying time of the blood at the post stenosis and this prolonging residence of time is considered to be dangerous for a patient with a stenosed artery. In this figure, we also see that the separation of the secondary shear layer from the lower wall is affected by the Reynolds number, e.g. when $Re = 1000$ the separation happens close to the centre, but for the other the Reynolds numbers the separation point moves slightly downstream. Furthermore, the interaction between the two shear layers create multiple vortex rolls close to the walls, the scenario is quite common for all the cases, but the vortex cells move further downstream when the Reynolds number increases.

More insight into the flow separation seen in Fig. 11 is given through the spanwise-averaged vorticity contours, $< \omega_z >_s = (\frac{\partial \bar{v}}{\partial x} - \frac{\partial \bar{u}}{\partial y})$, in Fig. 12. Two vortical structures form in the downstream region, one acts in the anti-clockwise direction shown by the dashed lines and the other is in the clockwise direction shown by the solid lines. The anti-clockwise vortex is initially formed from the nose of the stenosis where the flow separation begins, while the clockwise vortex is formed after $y/L = 1.0$ near the lower wall. Both of them interact with each other and then roll up to the downstream region. It is also evident from the colour legend that for $Re = 1000$ and 1400 the maximum magnitude of the clockwise vortices lies at the region of $2.0 < y/L < 4.0$, while for $Re = 1700$ and 2000 the maximum magnitude occurs after $y/L > 4.0$, which is plausible for the higher Reynolds number as the intensity

of the streamwise velocity is larger in these cases.

Fig. 13 illustrates the important physical quantity, namely, the wall shear stress, $\tau_{xy} = \mu(\frac{\partial \bar{v}}{\partial x} + \frac{\partial \bar{u}}{\partial y})/\rho \bar{V}^2$, plotted at the centreline along the streamwise direction in (a) the upper wall and (b) lower wall respectively. The acute shear stress drop which is found just prior to the centre of the stenosis in the upper wall has some important pathological concerns, as this usually induces an accelerated amount of intimal thickening of a blood vessel (Salam *et al.* [51]). The upper-wall shear stresses rise from the throat of the stenosis and attain a peak value in the region $1.0 < y/L < 2.0$. Though towards the further downstream the magnitudes drop gradually, they oscillate within the region of $1.0 < y/L < 6.0$. On the other hand, the rise of the shear stresses at the centre of the stenosis on the lower wall and the abnormal oscillating form due to the large turbulence intensity are quite harmful to a patient in the senses that they influence to causes damages to the red blood cells and the inner lining of an arterial vessel. This high shear stress may also overstimulate platelet thrombosis, causing a total occlusion (Folts *et al.* [52]) in blood vessel.

5.4 Mean flow characteristics

The mean streamwise velocity recorded at the different axial locations is presented in Fig. 14(a-n) for the deferent Reynolds numbers. The mean velocity, whose patterns in the inlet correspond to a fully developed laminar Poiseuille flow, increases rapidly in the post-stenotic region for all the Reynolds numbers, and the negative values occurring in the velocity near the upper wall correspond to the presence of the permanent re-circulation region seen in Figs. 9 and 15. However, towards the further downstream the velocity does not change significantly as the flow settles down there after the transient. Again, we see in Fig. 15 that the length of the re-circulation region increases with the Reynolds number since the intensity of the adverse pressure increases in the post-lip region (see Fig. 17a). Moreover, the acute pressure drop seen in Fig. 17 within the immediate post stenosis region could potentially cause a stroke as the blood in this region flows in the opposite direction owing to the reversal of the pressure gradients. The DNS (Case 6) results of the mean pressure for $Re = 2000$ have been compared with those of the LES and the agreement found is quite good indeed.

The instant results of the shear stresses have already been presented in Fig. 13 and discussed before, but it would be interesting to see now how their means vary in the post stenosis region. Fig. 16 presents the mean results of the shear stresses for the various Reynolds numbers, plotted at the (a) upper wall, (b) centreline, and (c) lower wall. The mean stresses at the upper wall show an abrupt drop just prior to the centre of the stenosis and have maximum after the immediate region of the post-lip as seen in Fig. 13(a). Also the rise of the mean shear stress at the lower wall coincides with the instant results (Fig. 13b), but the highly oscillatory nature that was found in the instant shear stresses is clearly absent here. The medical consequences of this oscillatory behaviour of the instant shear stresses have been pointed out in the previous section, in addition to those, the blood cells and the endothelial side of the blood vessels can experience the sharp rise and fall of the mean shear stresses in the post stenosis. The DNS results for $Re = 2000$ also show

an excellent agreement with those of the LES.

5.5 Turbulent characteristics

The root mean square (rms) of the streamwise velocity fluctuations, v''_{rms}, normalised by $\bar{V}$, are recorded at the different selected axial positions and depicted in Fig. 18 for $Re = 1000$, 1400, 1700 and 2000. The zero values of v''_{rms} at the inlet correspond to the laminar pulsatile flow, while the values of v''_{rms} grow slightly at the transitional stage which occurs at the centre of the stenosis, shown in (b) $y/L = 0.0$, The effect of the Reynolds numbers on v''_{rms} at the upstream of the stenosis is indistinctive. However, at the post stenotic region, in frames (c-e), the rise of the magnitude of v''_{rms} takes place near the upper wall where the stenosis appeared. Frames (f-j) show that the intensity of the streamwise velocity fluctuations slightly decreases near the upper wall but enhances near the lower wall. Towards the far downstream, frames (k-n), the flow is still turbulent but the intensity reduces gradually, since the further downstream region is working as the recovery zone. It is clear that these turbulent fluctuations are highly dependent on the presence of the stenosis as well as on the Reynolds number.

The total turbulent intensity, which is calibrated in terms of the turbulent kinetic energy (TKE), $\frac{1}{2} < u''_j u''_j > /\bar{V}^2$, is presented in Fig. 19 along the mid-centreline. From these figures it is clearly seen that the turbulent kinetic energy is negligible at the upstream region as well as before the post-lip of the stenosis, i.e. the random turbulent fluctuations are approximately zero due to the laminar and transient state of the flow. But the TKE increases from the centre of the stenosis as the transient flow becomes turbulent and the high level of TKE lies in the post stenosis region of $0.0 < y/L < 6.0$. In a pathological senses, these are quite important factors as they are responsible for damaging the blood cells and the tissues inside of a blood vessel. The effect of the Reynolds number on the magnitude of the TKE is also clearly visible. For example, the TKE grows with the Reynolds number, but at the far downstream region the turbulent characteristic is more universal and is independent to the Reynolds number. The coarse DNS (Case 6) results of the TKE and v''_{rms} (Fig. 18) for $Re = 2000$ show good agreement with those of the LES.

5.5.1 Cycle-to-cycle variations

The streamwise velocity, $\bar{v}/\bar{V}$, is plotted in Fig. 20 against the time, t/T, at the different axial positions y/L for $Re = 2000$. Note that the data was saved at the centre of the channel, i.e. at $x/L = z/L = 0.5$. The objectives here are to demonstrate clearly where, when and how the physiological flow becomes disturbed, and to present its cycle-to-cycle variations. At the centre of the stenosis (also at the upstream of the stenosis, not shown in the figure), frame (a) clearly shows that the flow pattern remains same at every cycle. But from the centre and towards the downstream of the stenosis, the flow is completely disturbed due to the presence of the stenosis. It would be noticed that the disturbance in the immediate downstream of the stenosis, in frames (b-d), is generated from the initial period of the time cycle, which then propagates to the further downstream, in frames (e-k), and remains perpetual at the rest of the cycles. However, the magnitude of the peak velocity

of the disturbed flow is different at the different streamwise locations and cycles, and the cycle-to-cycle variation of the velocity at the downstream is not periodic. The peak velocity is highly increased in the immediate downstream of the stenosis, around the region of the post-lip of the stenosis where the level of turbulence was recorded high, but the magnitude of the peak velocity drops gradually towards the further downstream, frames (l-o), because of the decaying of the turbulence.

The cycle-to-cycle variation of the pressure gradient of the flow field, which are recorded at the upper wall of the channel and presented in Fig. 21, reveals some additional important information of the disturbed flow downstream of the stenosis such that the highly oscillating pressure gradient that occurs at the immediate post stenotic region can cause arterial murmur sound. This important clinical issue will be discussed later in more details by means of the energy spectra of the pressure fluctuations.

5.5.2 Turbulent energy spectra

The energy spectra, $E_{\alpha''\alpha''}$ (here α represents a generic variable either fluctuating velocity or pressure), for the the streamwise velocity fluctuations, $(v''/\bar{V})^2$, and the pressure fluctuation, $(p''/\rho\bar{V}^2)^2$, for $Re = 2000$ are presented in Figs. 22 and 23, respectively, at different axial positions in the post stenosis region.

Fig. 22 shows the normalized turbulent energy spectra, $E_{v''v''} = E(f)\bar{V}/L$, for the centreline v-velocity fluctuations, $(v''/\bar{V})^2$, against the Strouhal number $Sr = fL/\bar{V}$ of the vortex shedding frequency f, where the frequency spectra, $E(f)$, has been computed by using the Fast Fourier Transform scheme. The straight lines corresponding to $Sr^{-5/3}$ and $Sr^{-10/3}$ are included in all the frames. In addition, only in frame (a) the $Sr^{-7/1}$ line is included to show a further break of frequency from $-10/3$ to $-7/1$. The energy spectra presented in this figure show the three important sub-range regions which match up closely with those of Tennekes and Lumley [53]. The two-stage decay in the slope of the turbulent flow spectra such as the inertial sub-range of slope $-5/3$ and the sub-range of $-10/3$ agree quite well with the experimental results of Gross *et al.* [54] and Lu *et al.* [55]. However, the region of the power spectra with the slope of $-7/1$ in the viscous dissipation range is found very small in our results and that is why it is included only in frame (a). Furthermore, the range of the inertia subrange region found in frames **??**(a-e) are approximately same, while it is very small in frames **??**(f-i) due to the small intensity of the turbulence found at the far downstream region (already discussed in the previous sections).

Fig. 23 presents the corresponding normalised energy spectra, $E_{p''p''}$, for the pressure fluctuations, $(p''^2/\rho\bar{V}^2)^2$, along with the straight lines of $Sr^{-5/3}$ and $Sr^{-7/3}$ to indicate respectively the inertia subrange region and the break-up of this region. In every frame the spectra containing the inertial/broadband region indicates the energy contained eddies of the turbulent flow in the post stenosis region. Due to the change of the slope from $-5/3$ to $-7/3$ the energy from the pressure fluctuations spectra transfers to the sound spectra which is a potential source of murmurs of the arterial stenosis. Moreover, likewise the velocity spectra, the broadband frequency found in frames (a-e) are larger than that of the spectra of slope $-7/3$, and in frame (f) the broadband region is very small where the turbulent intensity was

relatively low. After the region of slope $-7/3$, the spectra end with the slope of a horizontal line of Sr.

6 Conclusion

Large Eddy Simulation with a localized dynamic sub-grid model has been applied to the study of physiological pulsatile flow through a 3D model of asymmetric stenosis. The justification of using the LES in the study of physiological pulsatile flow in the model is made through the results of the SGS model. Particularly, we found when $Re = 2000$, the large scale motions receive a maximum of about 37.4% contribution from the SGS model. However, for the other Reynolds numbers less than 2000, this contribution is less since the intensity of the turbulence in the downstream of the stenosis drops when the Reynolds numbers is reduced.

A comparison of the results obtained by the LES is made with the coarse DNS, and an excellent agreement is found in the mean pressure and shear distributions. But some variations are seen in the turbulent characteristics, which is quite reasonable due to the effects of the subgrid models. For the different grid resolutions and timesteps used in the simulations, the turbulent intensities vary slightly but the mean results are quite resolved and independent to the grids and timesteps.

The nature of the instantaneous flow field at the post stenosis region is highly oscillating due to the physiological pulse and to the presence of the stenosis. It also be found that the upper-wall shear stress drop which takes place at the centre of the stenosis is completely opposite to the results of Mittal *et al*. [30] who studied the pulsatile flow by LES in a planar channel with a semi-circular type constriction.

We have also found that the flow characteristics, the turbulent kinetic energy, the root mean square of the turbulent fluctuations, etc, are highly dependent on the flow Reynolds number, and they are enhanced by the increment of the Reynolds number. The maximum turbulent kinetic energy occurs not in the centre of the channel but near the upper wall where the stenosis appeared. We have highlighted the fact that the high level of the turbulent fluctuations found in the downstream ($0 < y/L < 6$) of the stenosis could activate the blood platelets and also damage the blood cell materials, and consequently they could create many pathological diseases. Further, the break frequency of the energy spectra from $-5/3$ to $-10/3$ for the velocity fluctuations and from $-5/3$ to $-7/3$ instead of $-10/3$ for the pressure fluctuations are observed in the immediate downstream region of the stenosis. The pathological consequences of this including the issues of murmur sound generated by the arterial stenosis are discussed in the paper.

Some limitations are acknowledged in the present study: (i) A simple model of stenosis formed on the top-wall of a channel has been studied whereas a real biological geometry/artery is usually cylindrical. (ii) The flow investigated is laminar pulsatile before the stenosis, in-vivo flows in the large arteries are spiral laminar due to the twisting nature of the heart pump [56]. (iii) The stenosis in the present investigation is eccentrically placed but pathological atherosclerotic stenosis are usually complex and a form of concentric narrowing with eccentric and irregular elements. (iv) The wall of the model are rigid unlike biological vessels which exhibit elasticity though this reduces with rising disease burden. The LES code is being extended

to overcome these limitations, however, we believe that despite the simplicity in the model the results presented in the paper would provide an insightful information and knowledge to understand a real (asymmetric) stenotic flow.

Acknowledgements

Funding from the Faculty of Engineering of the University of Glasgow and from the ORSAS are acknowledged gratefully by the first author. The authors also thank the anonymous reviewers for their valuable comments and suggestions on the earlier version of this paper, which have served to improve the manuscript.

References

[1] D. N. Ku, Blood flows in arteries, Annu. Rev. Fluid Mech. 29 (1997) 399–434.

[2] R. S. Lees, C. F. Dewey, Phonoangiography: a new noninvasive diagnostic method for studying arterial disease, Proc. Nat. Ac. Sci. 67(2),October (1970) 935–942.

[3] C. Clark, Turbulent velocity measurements in a model of aortic stenosis, J. Biomech. 9 (1976) 677–687.

[4] C. Clark, Turbulent wall pressure measurements in a model of aortic stenosis, J. Biomech. 10 (1977) 461–472.

[5] R. J. Tobin, I.-D. Chang, Wall pressure spectra scaling downstream of stenosis in steady tube flow, J. Biomech. 9 (1976) 633–640.

[6] A. M. A. Khalifa, D. P. Giddens, Analysis of disorder in pulsatile flows with application to poststenotic blood velocity measurement in dogs, J. Biomech. 11 (1978) 129–141.

[7] A. M. A. Khalifa, D. P. Giddens, Characterization and evolution of poststenotic flow disturbances, J. Biomech. 14, no. 5 (1981) 279–296.

[8] S. A. Ahmed, D. P. Giddens, Velocity measurement in steady flow through axisymmetric stenosis at moderate Reynolds number, J. Biomech. 16, no. 7 (1983) 505–516.

[9] S. A. Ahmed, D. P. Giddens, Flow disturbances measurements through a constricted tube at moderate Reynolds number, J. Biomech. 16, no. 12 (1983) 955–963.

[10] S. A. Ahmed, D. P. Giddens, Pulsatile poststenotic flow studies with Laser Doppler Anemometer, J. Biomech. 17, no. 9 (1984) 695–705.

[11] S. A. Ahmed, An experimental investigation of pulsatile flow through a smooth constriction, Exp. Therm. Fluid Sci. 17 (1998) 309–318.

[12] V. O'Brien, L. Ehrlich, I. Simple pulsatile flow in an artery with a constriction, J. Biomech. 18(2) (1985) 117–127.

[13] O. R. Tutty, Pulsatile flow in a constricted channel, J. Biomech. Eng. 114 (1992) 50–54.

[14] C. Tu, M. Delville, L. Dheur, L. Vanderschure, Finite element simulation of pulsatile flow throgh arterial stenosis, J. Biomech. 25 (1992) 1141–1152.

[15] V. Deplano, M. Siouffi, Experimental and numerical study of pulsatile flows through stenosis: Wall shear stress analysis, J. Biomech. 32 (1999) 1081–1090.

[16] V. Damodaran, G. W. Rankin, C. Zhang, Numerical study of steady laminar flow through tube with multiple constriction using curvilinear co-ordinates, Int. J. Numer. Meth. Fluids 23 (1996) 1021–1041.

[17] G. R. Zendehbudi, M. S. Moayeri, Comparison of physiogical and simple pulsatile flows through stenosed ateries, J. Biomech. 32 (1999) 959–965.

[18] A. S. Dvinsky, M. Ojha, Simulation of three-dimensional pulsatile flow through an asymmetric stenosis, Med. Biol. Eng. Comput. 32 (1994) 138–142.

[19] J. R. Buchanan, C. Kleinstreuer, J. K. Comer, Rheological effects on pulsatile hemodynamics in a stenosed tube, Comput. Fluids 29 (2000) 695–724.

[20] Q. Long, X. Y. Xu, K. V. Ramnarine, P. Hoskins, Numerical investigation of physiological realistic pulsatile flow through arterial stenosis, J. Biomech. 34 (2001) 1229–1242.

[21] P. Neofytou, S. Tsangaris, Flow effects of blood constitutive equations in 3D models of vascular anomalies, Int. J. Numer. Meth. Fluids 51 (2006) 489–510.

[22] F. Mallinger, D. Drikakis, Laminar-to-turbulent transition in pulsatile flow through a stenosis, Biorheology 39 (2002) 437–441.

[23] F. Mallinger, D. Drikakis, Instability in three-dimensional, unsteady, stenotic flows, Int. J. Heat and Fluid Flow 23 (2002) 657–663.

[24] F. Ghalichi, X. Deng, A. D. Champlain, Y. Douville, M. King, R. Guidoin, Low Reynolds number turbulence modeling of blood flow in arterial stenosis, Biorheology 35, no. 4,5 (1998) 281–294.

[25] T. S. Lee, W. Liao, H. T. Low, Numerical simulation of turbulent flow through series stenoses, Int. J. Numer. Meth. Fluids 42 (2003) 717–740.

[26] T. S. Lee, W. Liao, H. T. Low, Numerical study of physiological turbulent flows through series arterial stenoses, Int. J. Numer. Meth. Fluids 46 (2004) 315–344.

[27] A. Scotti, U. Piomelli, Turbulence models in pulsatile flow, AIAA Journal 40 (3) (2002) 537–544.

[28] M. C. Paul, M. M. Molla, G. Roditi, Large-eddy simulation of pulsatile blood flow, Medical Engineering Physics 31 (2009) 153–159.

[29] M. M. Molla, M. C. Paul, G. Roditi, Les of additive and non-additive pulsatile flows in a model arterial stenosis, Comp. Meth. Biomech. Biomed. Eng 13 (2010) 105–120.

[30] R. Mittal, S. P. Simmons, F. Najjar, Numerical study of pulsatile flow in a constricted channel, J. Fluid Mech. 485 (2003) 337–378.

[31] U. Piomelli, J. Liu, Large-eddy simulation of rotating channels flows using a localized dynamic model, Phys. Fluids 7 (4) (1994) 839–847.

[32] M. D. Deshpande, D. P. Giddense, R. F. Mabon, Steady laminar flow through modelled vascular stenosis, J. Biomech. 9 (1976) 165–174.

[33] T. J. Pedley, The fluid mechanics of large blood vessels, Cambridge University Press, 1980.

[34] J. Smagorinsky, General circulation experiment with the primitive equations. i. the basic experiment, Monthly Weather Rev. 91 (1963) 99–164.

[35] J. R. Womersley, Method for the calculation of velocity, rate of flow and viscous drag in arteris when the pressure gradient is known, J. Physiol. 155 (1955) 553–563.

[36] C. Loudon, A. Tordesillas, The use of the dimensionless Womersley number to characterize the unsteady nature of internal flow, J. theor. Biol. 191 (1998) 63–78.

[37] Y. Morinishi, Conservation prperties of finite difference schemes for incompressible flow, Center for Turbulence Research, (1995) 121–132.

[38] S. V. Patankar, Numerical heat transfer and fluid fow, Hemisphere Publishing Corporation, 1980.

[39] C. M. Rhie, W. L. Chow, Numerical study of the turbulent flow past an airfoil with trailing edge separation, AIAA J. 21(11) (1983) 1525–1532.

[40] H. A. D. Vorst, BI-CGSTAB: a first and smoothly converging variant of BI-CG for the solution of the non-symmetric linear systems, SIAM J. Sci. Stat. Comput. 13 (2) (1992) 631–644.

[41] D. S. Kershaw, The Incomplete Cholesky-Cojugate Gradient method for the iterative solution of systems, J. Com. Phys. 26 (1978) 43–65.

[42] W. P. Jones, M. Wille, Large-eddy simulation of a plane jet in a cross-flow, Int. J. Heat and Fluid flow 17 (1996) 296–306.

[43] L. di Mare, W. P. Jones, LES of turbulent flow past a swept fence, Int. J. Heat and Fluid Flow 24 (2003) 606–615.

[44] W. P. Jones, M. C. Paul, Combination of DOM with LES in a gas turbine combustor, Int. J. Engineering Science 43 (6) (2006) 379–397.

[45] M. C. Paul, Performance of the various Sn approximations of DOM in a 3D combustion chamber, ASME J. Heat Transfer 103 (7) (2008) 072701–1–7.

[46] M. M. Molla, Large eddy simulation of pulsatile flow in the models of arterial stenosis and aneurysm, PhD thesis 2009, University of Glasgow, UK.

[47] A. K. M. Hussain, W. C. Reynolds, The mechanics of an organized wave in turbulent shear flow, J. Fluid. Mech. 41, part 2 (1970) 241–258.

[48] B. B. Lieber, D. P. Giddens, Post-stenotic core flow behavior in pulsatile flow and its effects on wall shear stress, J. Biomech. 23, no. 6 (1990) 597–605.

[49] H. Choi, P. Moin, Effect of the computational time step on numerical solutions of turbulent flow, J. Computational Physics, 111 (1994) 1–4.

[50] A. Frydrychowicz, A. Harloff, B. Jung, M. Zaitsev, E. W. Eigang, T. A. Bley, M. Langer, J. Henning, M. Markl, Time-resolved, 3-dimensional magnetic resonance flow analysis at 3 T: visualization of normal and pathological aortic vascular hemodynamics, J. Comput. Assist. Tomogr. 31(1) (2007) 9–15.

[51] T. A. Salam, A. B. Lumsden, W. D. Suggs, D. N. Ku, Low shear stress promotes intinmal hyperplasia thickening, J. Vasc. Invest. 2 (1996) 12–22.

[52] J. D. Folts, E. B. Crowell, G. G. Rowe, Platelet occlusion. platelet aggregation in partially obstructed vessels and its elimination with aspirin, Circulation 54 (1976) 365–370.

[53] H. Tennekes, J. L. Lumley, A first course in turbulence, The MIT press, 1972.

[54] D. R. Gross, P. Lu, K. T. Dodd, H. C. Hwang, Physical characteristics of pulmonary artery stenosis murmurs in claves, Am. J. Physiol. 238 (Heart Circ. Physiol. 7) (1980) H876–H885.

[55] P. C. Lu, D. R. Gross, H. C. Hwang, Intravascular pressure and velocity fluctuations in palmonic arterial stenosis, J. Biomech. 13 (1980) 291–300.

[56] M. C. Paul, A. Larman, Investigation of spiral blood flow in a model of arterial stenosis, Med Eng and Phys, 31 (2009) 1195–1203.

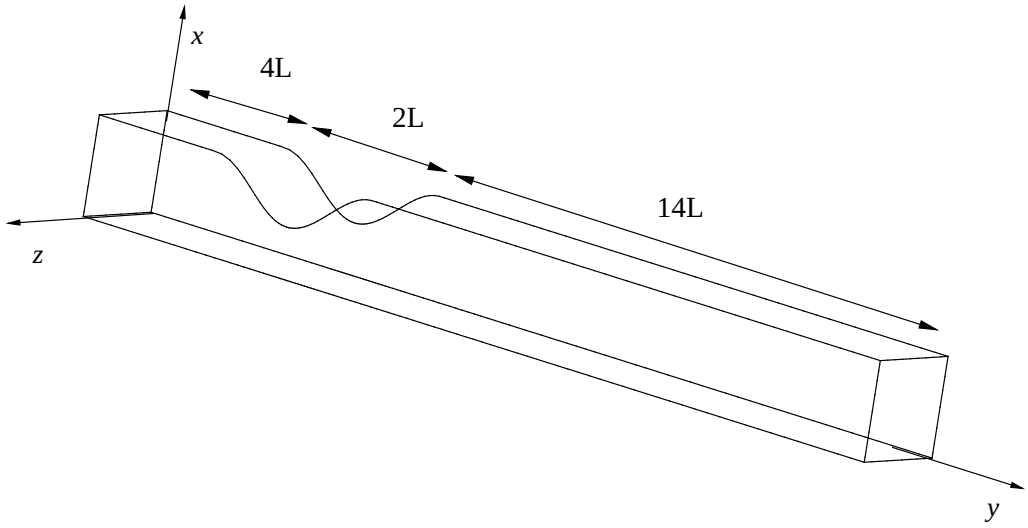

Figure 1: A schematic of the model with coordinate system.

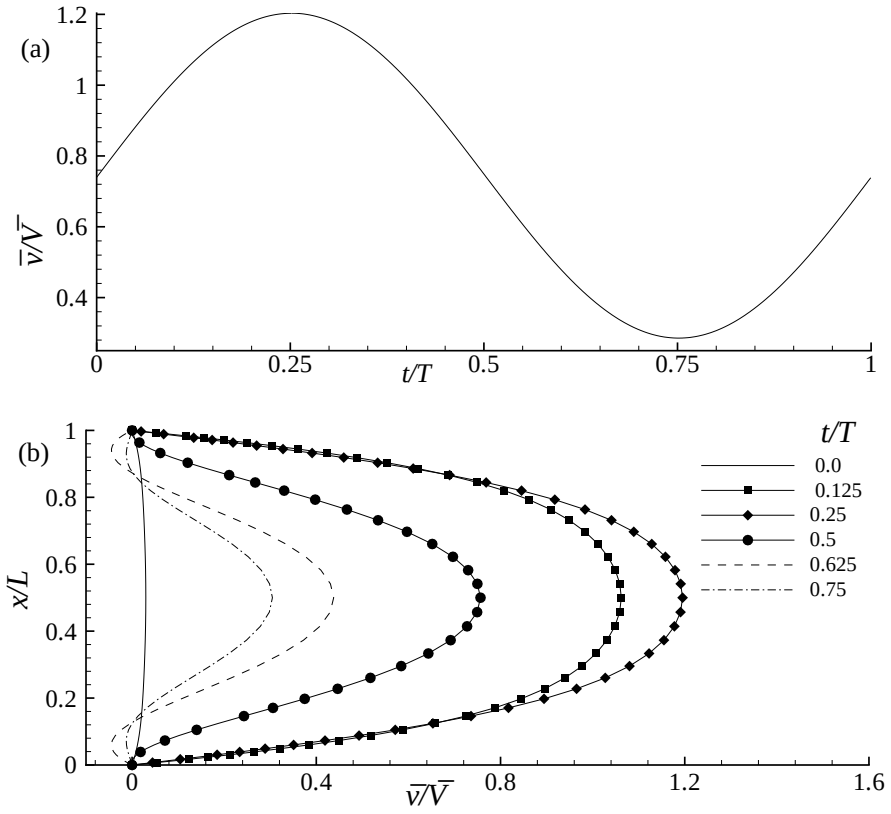

Figure 2: Inlet velocity profile for $Re = 2000$ and $\alpha = 10.5$ recorded (a) at the centre of the inlet plate during a full pulsation, and (b) between the top and bottom plates at different times.

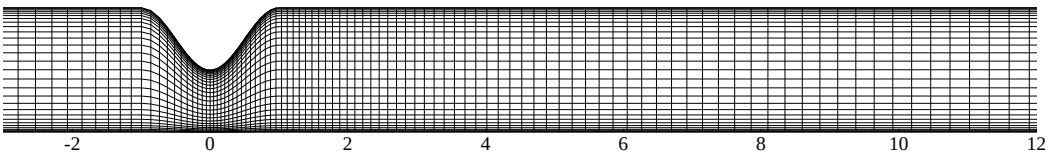

Figure 3: A crude mesh distribution in the $x - y$ plane.

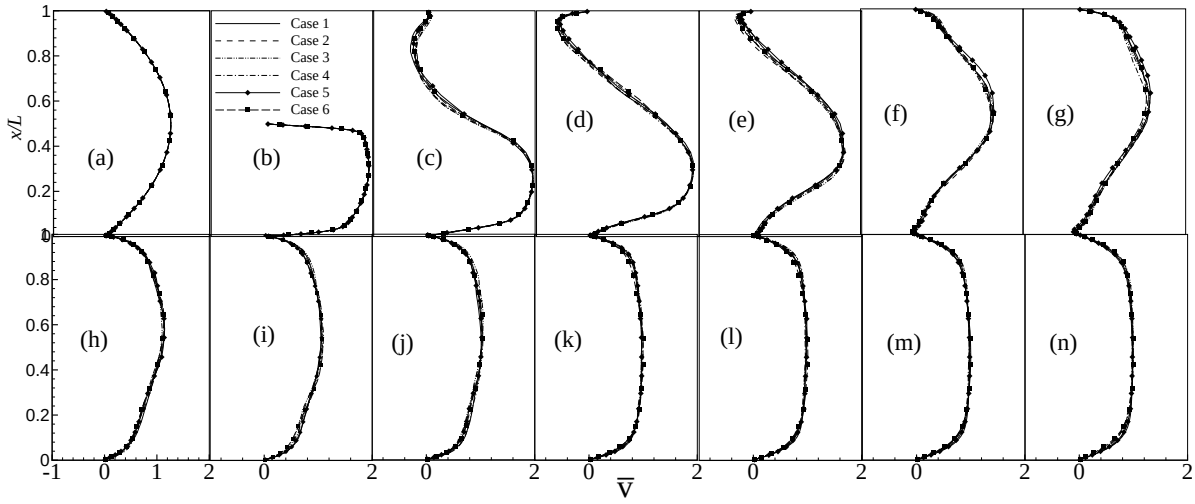

Figure 4: Grid independence test for the mean streamwise velocity, $< \bar{v} > /\bar{V}$ at (a) $y/L =$ inlet, (b) $y/L = 0.0$, (c) $y/L = 1.0$, (d) $y/L = 1.5$, (e) $y/L = 2.0$, (f) $y/L = 2.5$, (g) $y/L = 3.0$, (h) $y/L = 4.0$, (i) $y/L = 5.0$, (j) $y/L = 6.0$, (k) $y/L = 8.0$, (l) $y/L = 10.0$, (m) $y/L = 12.0$ and (n) $y/L =$ outlet, while $Re = 2000$.

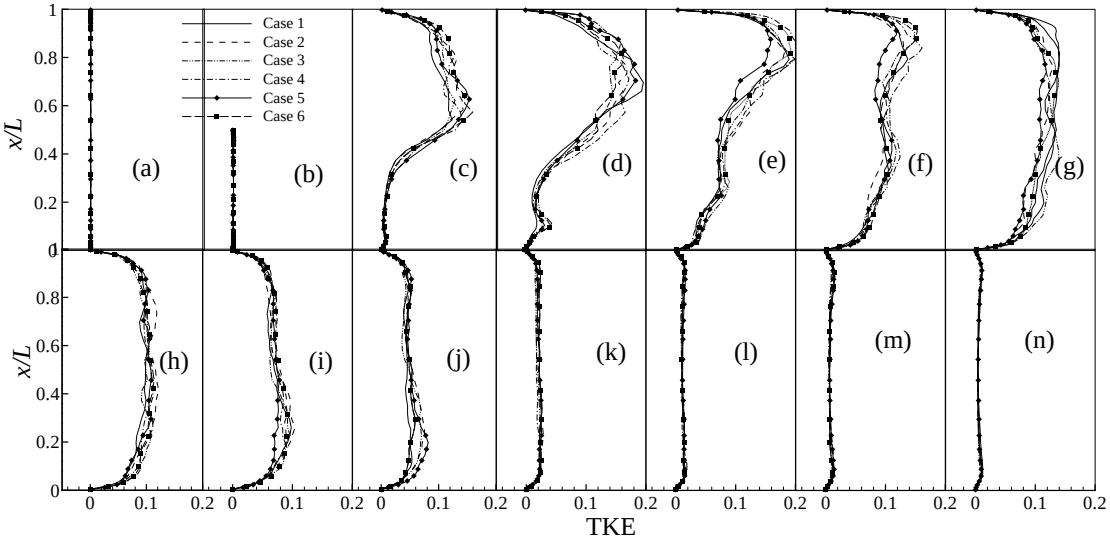

Figure 5: Grid independence test for the turbulent kinetic energy (TKE), $\frac{1}{2} < u_j'' u_j'' > /\bar{V}^2$, at (a) $y/L =$ inlet, (b) $y/L = 0.0$, (c) $y/L = 1.0$, (d) $y/L = 1.5$, (e) $y/L = 2.0$, (f) $y/L = 2.5$, (g) $y/L = 3.0$, (h) $y/L = 4.0$, (i) $y/L = 5.0$, (j) $y/L = 6.0$, (k) $y/L = 8.0$, (l) $y/L = 10.0$, (m) $y/L = 12.0$ and (n) $y/L =$ outlet, while $Re = 2000$.

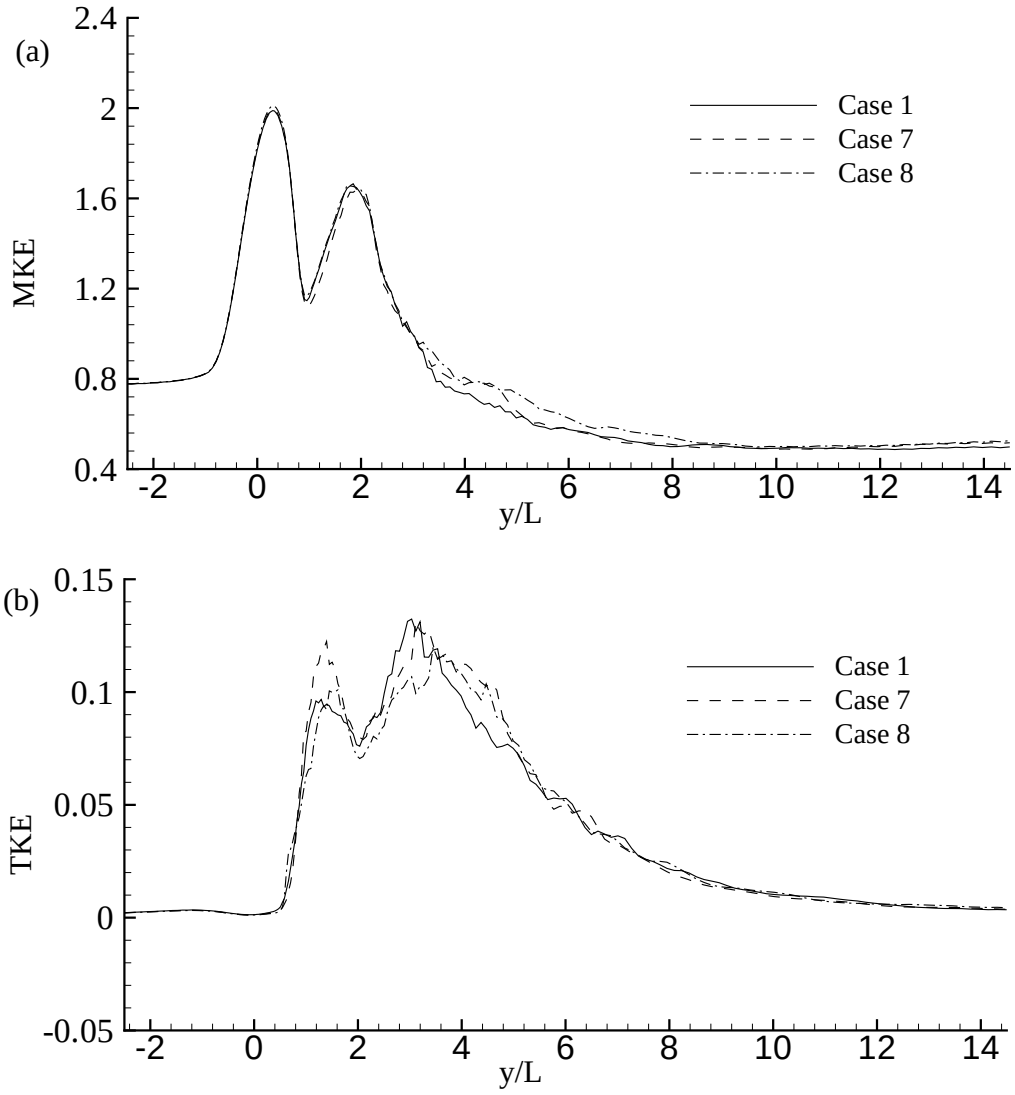

Figure 6: Timestep independence test for the (a) mean kinetic energy (MKE), $\frac{1}{2} < \bar{u}_j \bar{u}_j > /\bar{V}^2$, and (b) turbulent kinetic energy (TKE), $\frac{1}{2} < u_j'' u_j'' > /\bar{V}^2$, while $Re = 2000$.

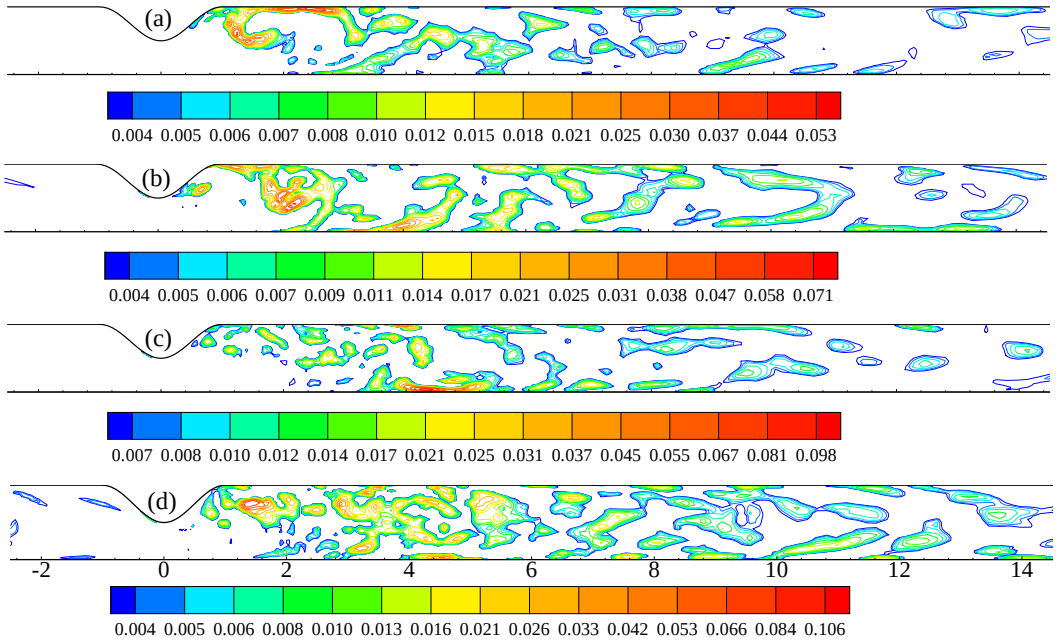

Figure 7: Dynamic Smagorinsky constant, C_s, saved at $t/T = 10.25$ for (a) $Re = 1000$, (b) $Re = 1400$, (c) $Re = 1700$ and (d) $Re = 2000$.

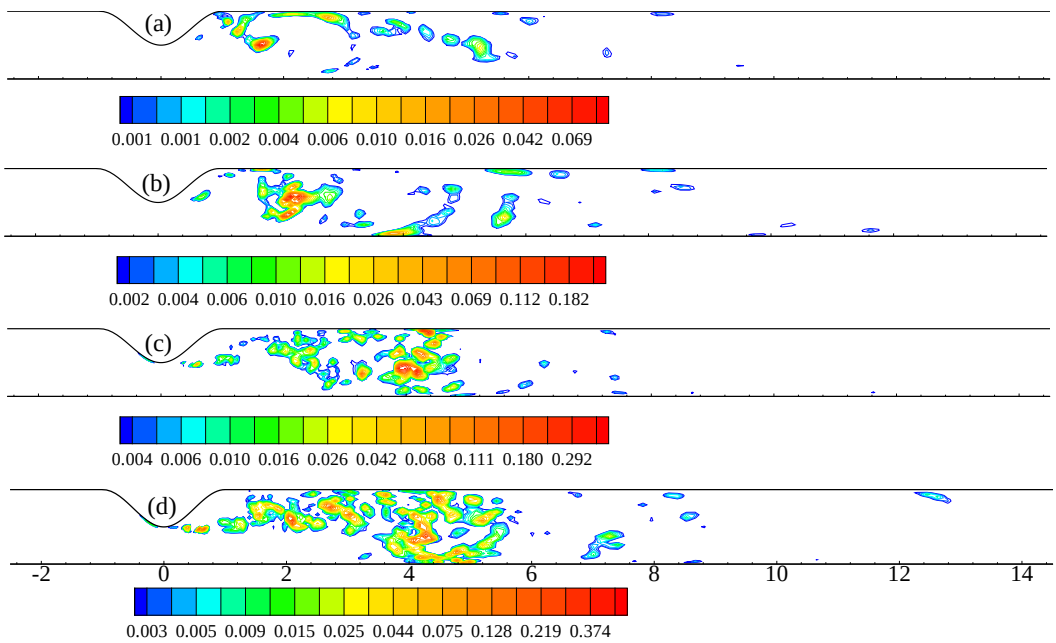

Figure 8: Normalised SGS eddy viscosity, μ_{sgs}/μ, saved at $t/T = 10.25$ for (a) $Re = 1000$, (b) $Re = 1400$, (c) $Re = 1700$ and (d) $Re = 2000$.

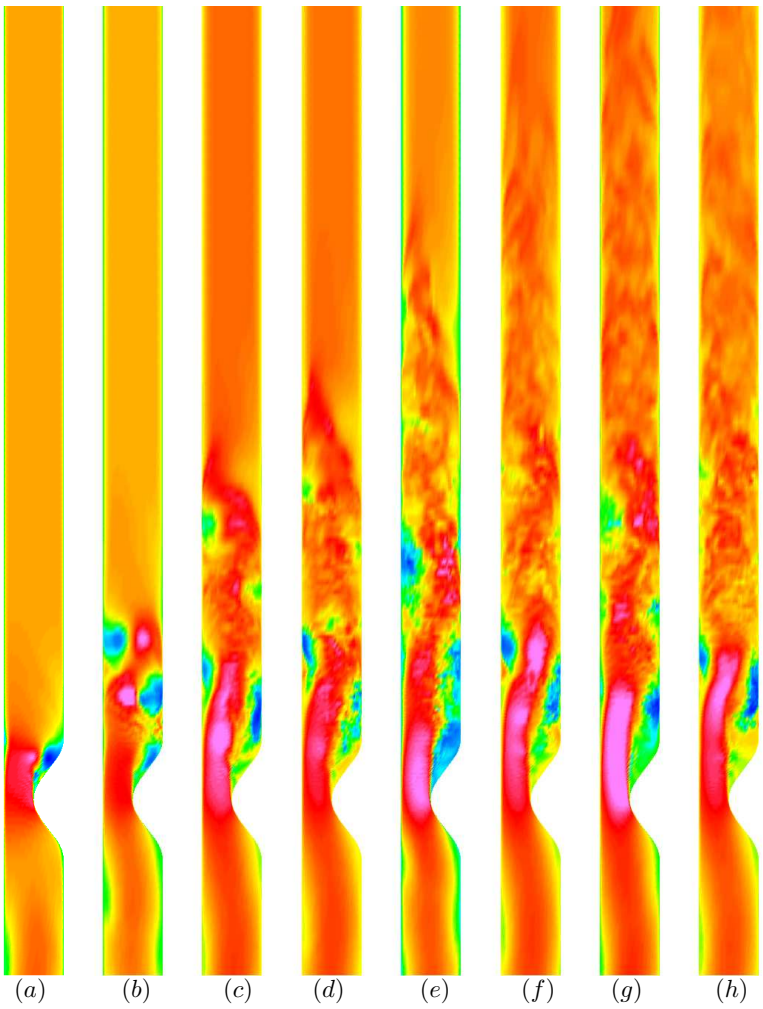

Figure 9: Streamwise velocity, $\bar{v}$, at (a) $t/T = 1.0$, (b) $t/T = 2.0$, (c) $t/T = 3.0$, (d) $t/T = 4.0$, (e) $t/T = 5.0$, (f) $t/T = 6.0$, (g) $t/T = 7.0$ and (h) $t/T = 8.0$ while $Re = 2000$.

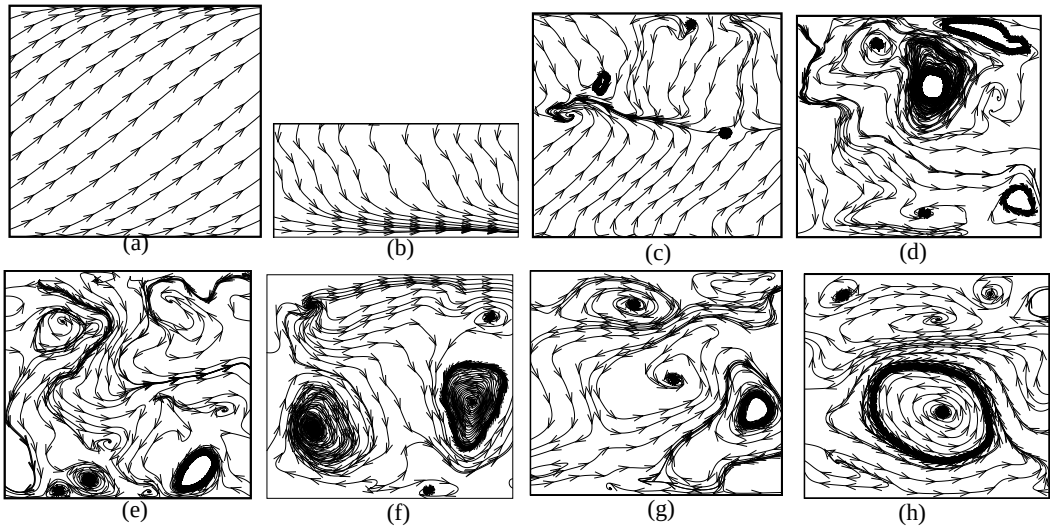

Figure 10: Instantaneous cross-sectional streamlines plotted at (a) $y/L = inlet$, (b) $y/L = 0$, (c) $y/L = 1$, (d) $y/L = 2$, (e) $y/L = 4$, (f) $y/L = 6$, (g) $y/L = 10$, and (h) $y/L = outlet$ while $Re = 2000$ and $t/T = 10.25$.

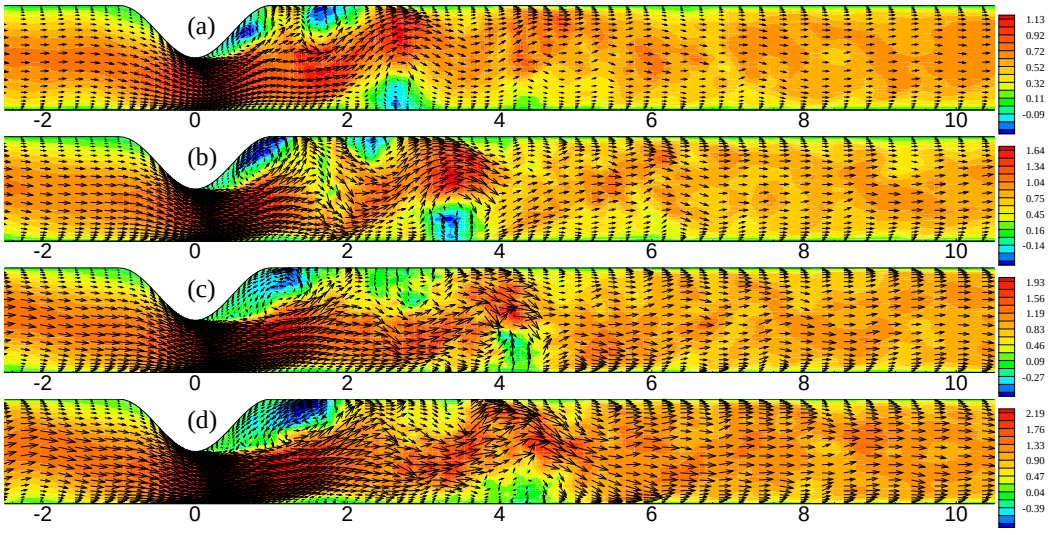

Figure 11: Instantaneous streamwise vectors appended on the streamwise velocity, $\bar{v}/\bar{V}$, at $t/T = 10.25$ for (a) $Re = 1000$, (b) $Re = 1400$, (c) $Re = 1700$, and (d) $Re = 2000$.

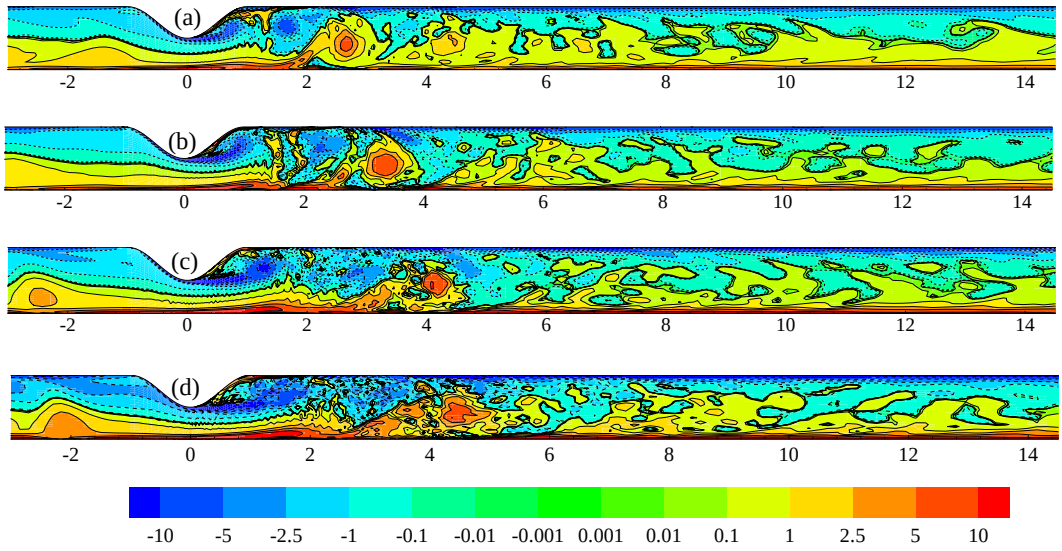

Figure 12: Spanwise average vorticity, $< \omega_z >_s$, for (a) $Re = 1000$, (b) $Re = 1400$, (c) $Re = 1700$, and (d) $Re = 2000$ at $t/T = 10.25$.

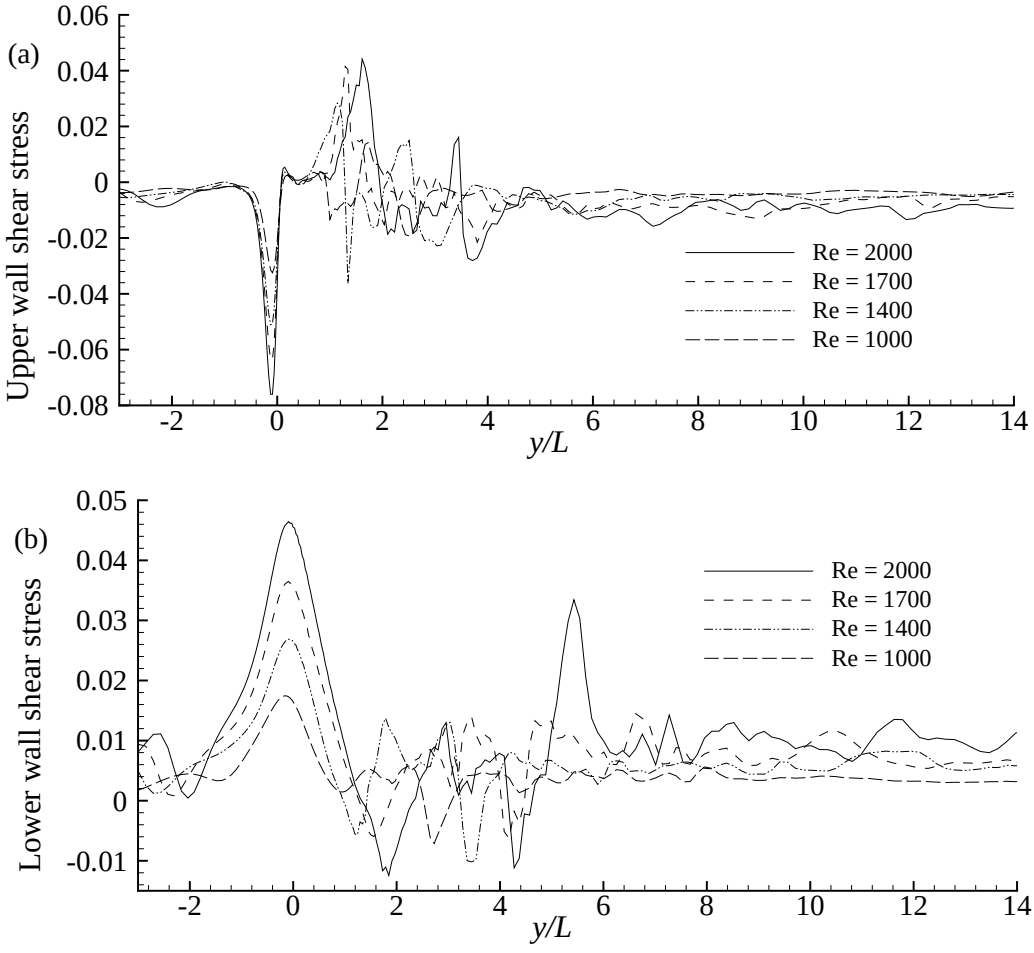

Figure 13: Instantaneous wall shearing stress,$\tau_{xy}/\rho\bar{V}^2$, at the (a) upper wall and (b) lower wall for the different Reynolds numbers while $t/T = 10.25$.

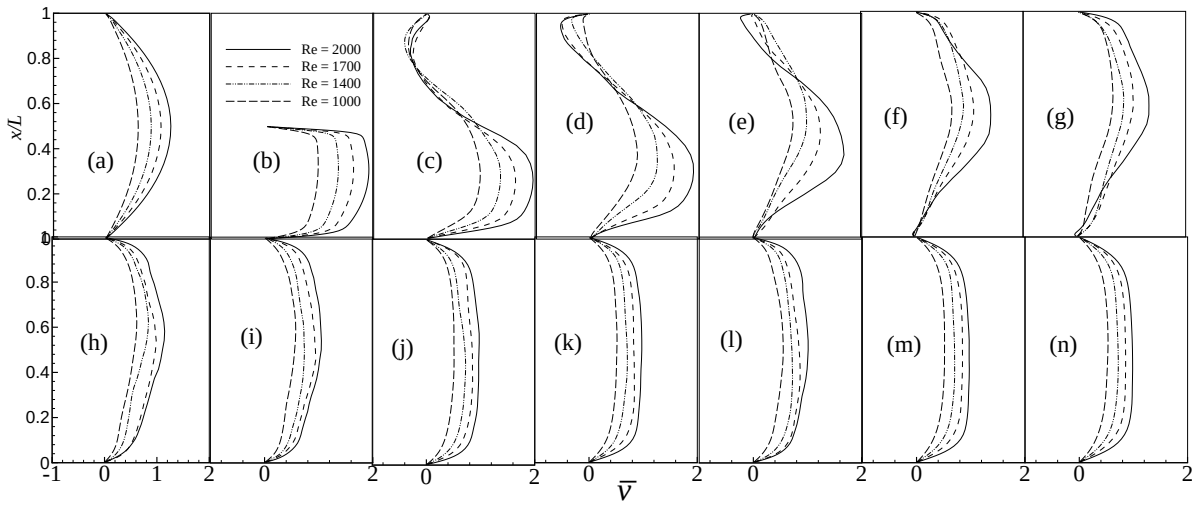

Figure 14: Mean streamwise velocity, $< \bar{v} > /\bar{V}$, at (a) $y/L =$ inlet, (b) $y/L = 0.0$, (c) $y/L = 1.0$, (d) $y/L = 1.5$, (e) $y/L = 2.0$, (f) $y/L = 2.5$, (g) $y/L = 3.0$, (h) $y/L = 4.0$, (i) $y/L = 5.0$, (j) $y/L = 6.0$, (k) $y/L = 8.0$, (l) $y/L = 10.0$, (m) $y/L = 12.0$ and (n) $y/L =$ outlet for the different Reynolds numbers.

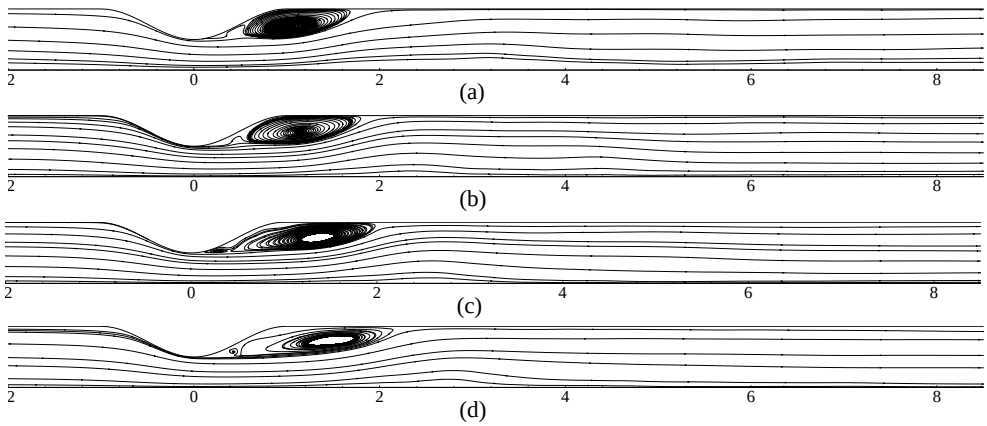

Figure 15: Mean streamlines for (a) $Re = 1000$, (b) $Re = 1400$, (c) $Re = 1700$, and (d) $Re = 2000$.

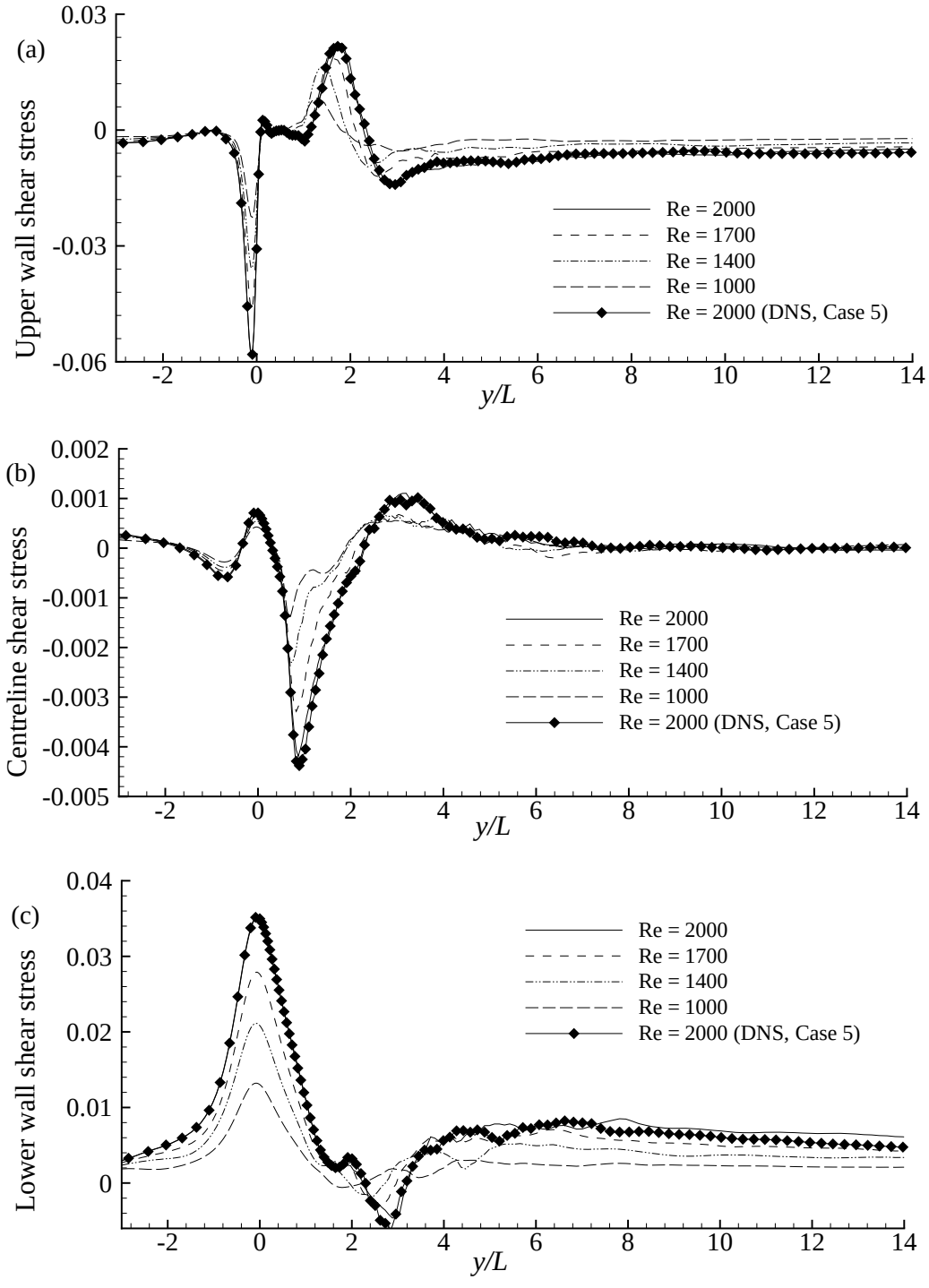

Figure 16: Mean shear stresses at the (a) upper wall (b) centreline and (c) lower wall for the different Reynolds numbers.

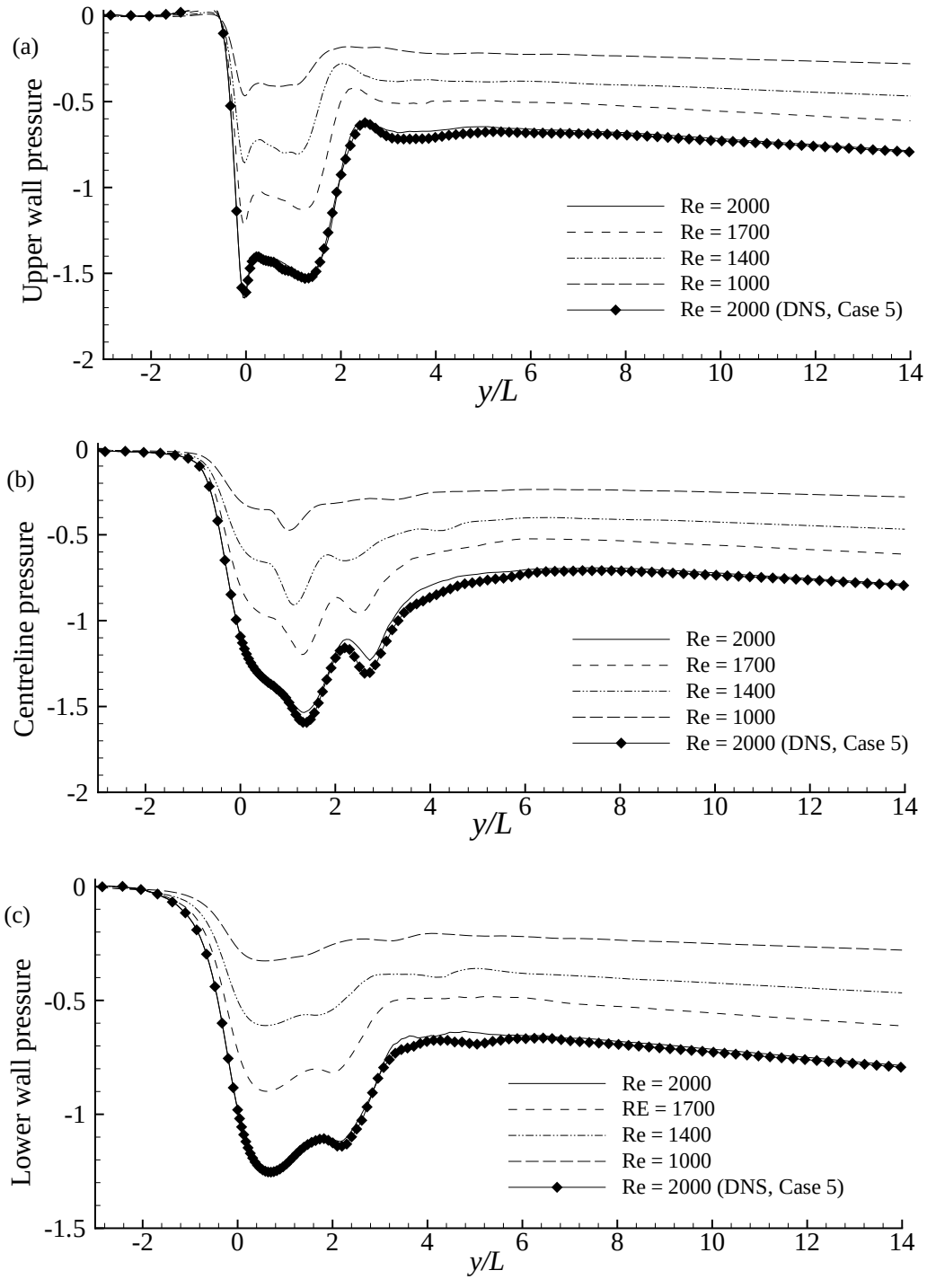

Figure 17: Mean pressure at the (a) upper wall (b) centreline and (c) lower wall for the different Reynolds numbers.

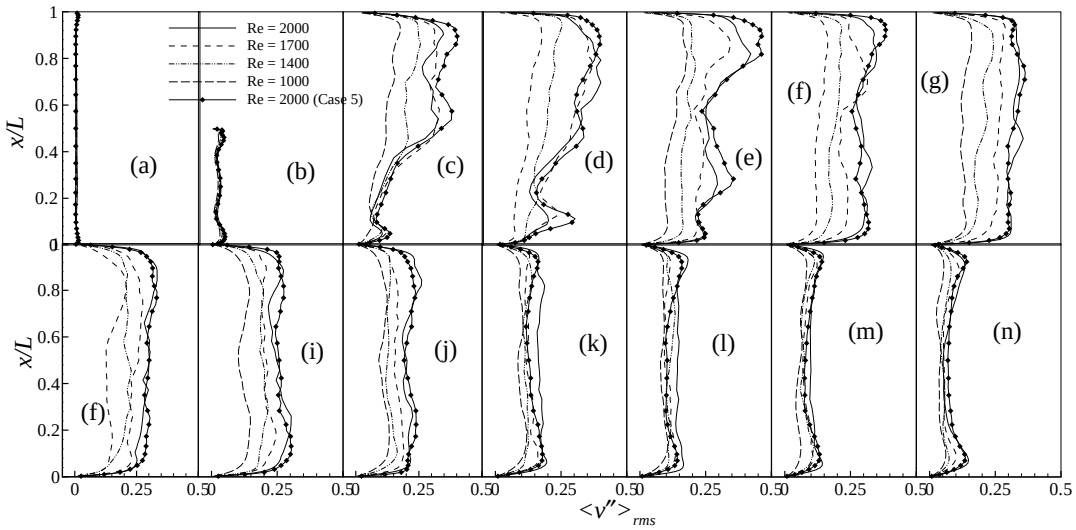

Figure 18: rms of the streamwise velocity fluctuations, $< v'' >_{rms} /\bar{V}$, at the different axial location, (a) $y/L =$ inlet, (b) $y/L = 0.0$, (c) $y/L = 1.0$, (d) $y/L = 1.5$, (e) $y/L = 2$, (f) $y/L = 2.5$, (g) $y/L = 3.0$, (h) $y/L = 4.0$, (i) $y/L = 5.0$, (j) $y/L = 6.0$, (k) $y/L = 8.0$ (l) $y/L = 10.0$, (m) $y/L = 12.0$ and (n) $y/L =$ outlet, for the different Reynolds numbers.

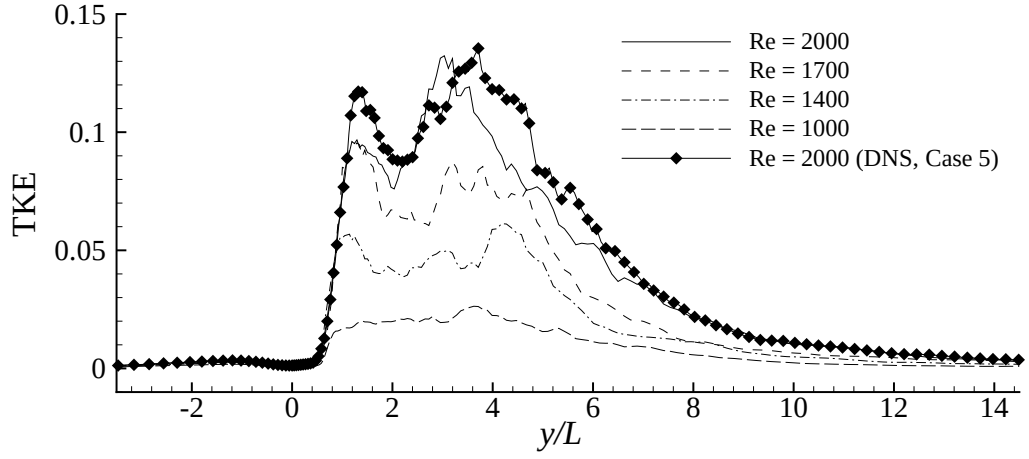

Figure 19: Centreline turbulent kinetic energy for the different Reynolds numbers.

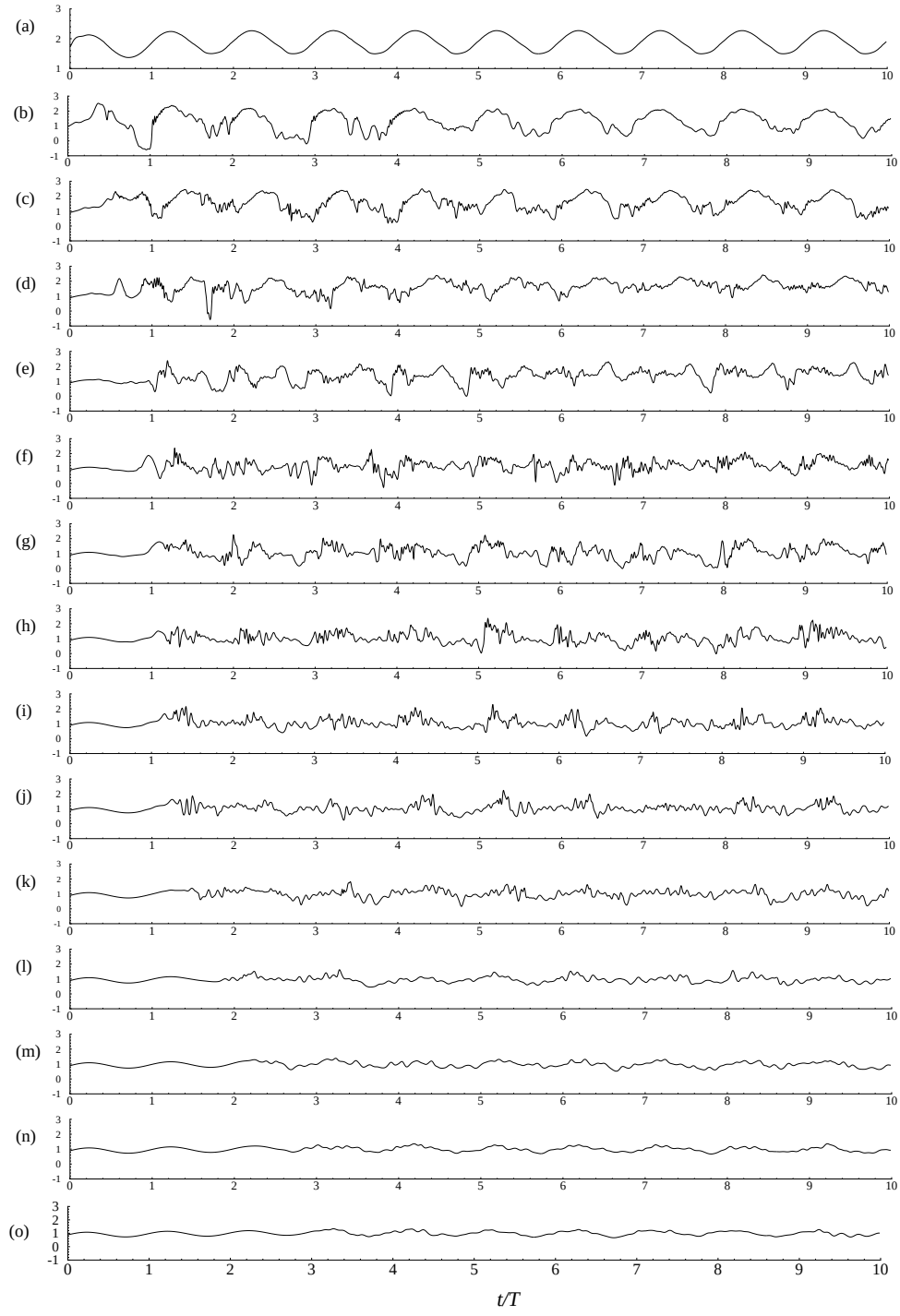

Figure 20: Time history of the streamwise centreline velocity, $\bar{v}/\bar{V}$, at (a) $y/L = 0.0$, (b) $y/L = 1.0$, (c) $y/L = 1.5$, (d) $y/L = 2.0$, (e) $y/L = 2.5$, (f) $y/L = 3.0$, (g) $y/L = 3.5$, (h) $y/L = 4.0$, (i) $y/L = 4.5$, (j) $y/L = 5.0$, (k) $y/L = 6.0$, (l) $y/L = 7.0$, (m) $y/L = 8.0$, (n) $y/L = 10.0$, and (o) $y/L =$outlet, while $Re = 2000$.

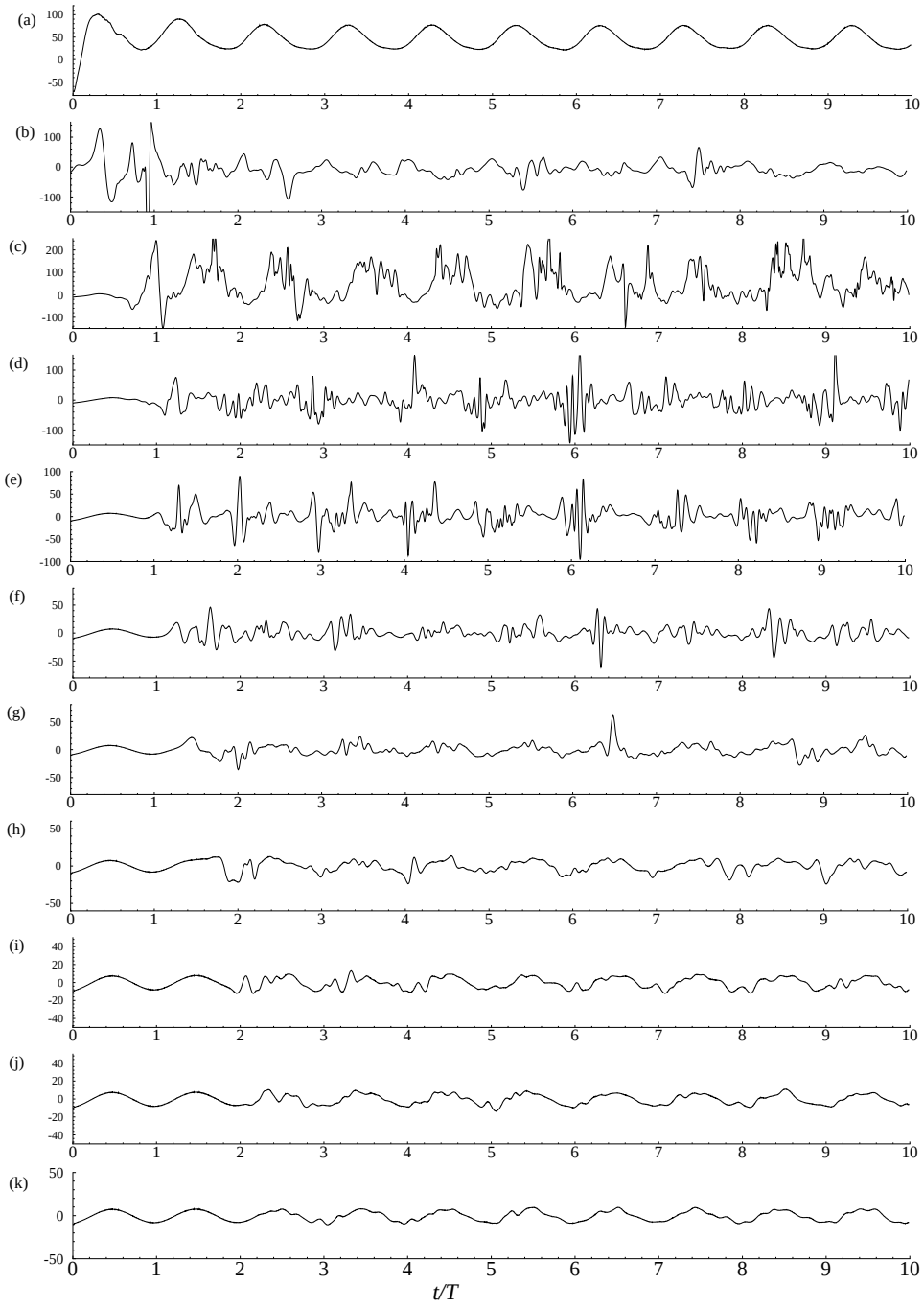

Figure 21: Time history of the upper wall pressure gradient, $\frac{\partial \bar{P}}{\partial y}$, at (a) $y/L = 0.0$, (b) $y/L = 1.0$, (c) $y/L = 2.0$, (d) $y/L = 3.0$, (e) $y/L = 4.0$, (f) $y/L = 5.0$, (g) $y/L = 6.0$, (h) $y/L = 7.0$, (i) $y/L = 8.0$, (j) $y/L = 9.0$, and (k) $y/L = 10.0$ while $Re = 2000$.

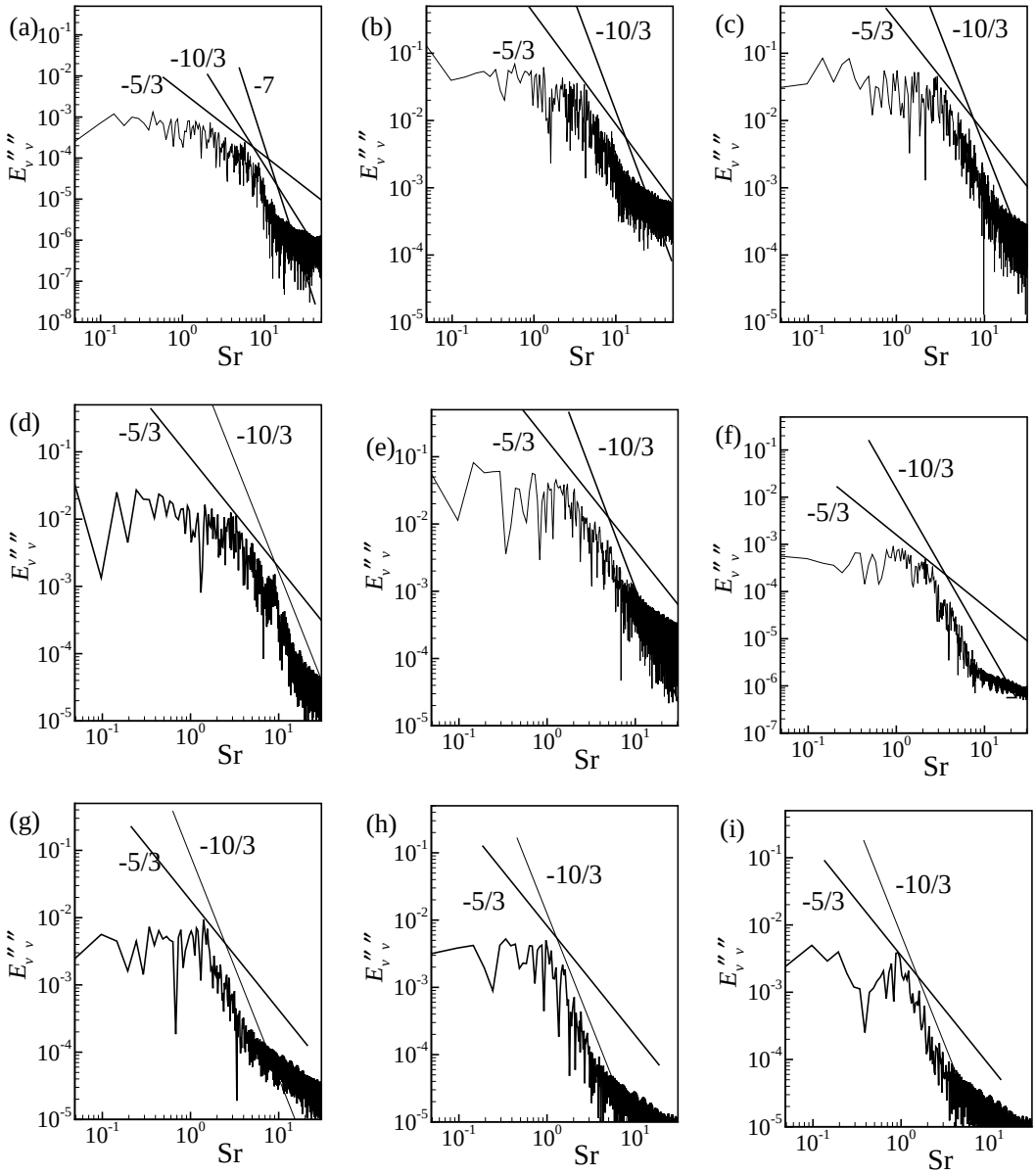

Figure 22: Energy spectrum of, v'', at (a) $y/L = 1.0$, (b) $y/L = 2.0$, (c) $y/L = 3.0$, (d) $y/L = 4.0$, (e) $y/L = 5.0$, (f) $y/L = 6.0$, (g) $y/L = 8.0$, (h) $y/L = 10.0$ and (i) $y/L = 12.0$ while $Re = 2000$.

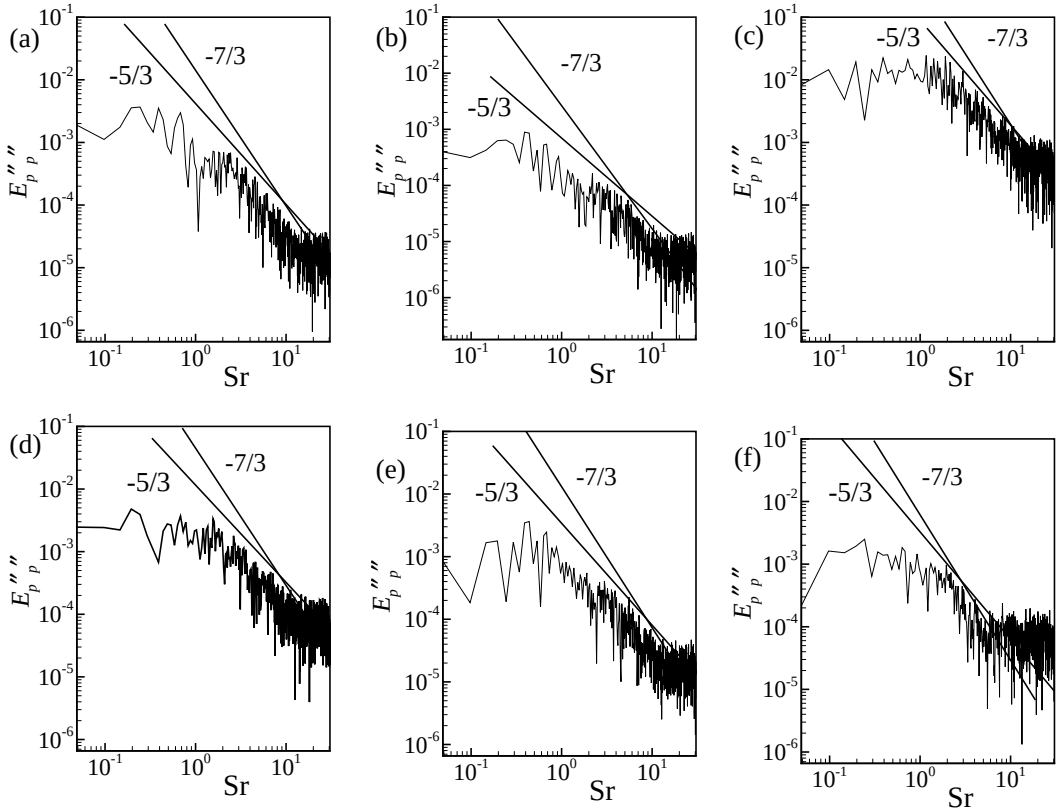

Figure 23: Energy spectrum of p'' at (a) $y/L = 1.0$, (b) $y/L = 2.0$, (c) $y/L = 3.0$, (d) $y/L = 4.0$, (e) $y/L = 5.0$ and (f) $y/L = 6.0$ while $Re = 2000$.